JOURNAL OF GEOPHYSICAL RESEARCH, VOL. 96, NO. C8, PAGES 14,995–15,016, AUGUST 15, 1991

Dynamics of the Coastal Transition Zone Jet 2. Nonlinear Finite Amplitude Behavior

J. S. ALLEN, LEONARD J. WALSTAD, AND P. A. NEWBERGER

College of Oceanography, Oregon State University, Corvallis

The finite amplitude nonlinear behavior of the coastal transition zone (CTZ) jet, assumed to be governed by quasi-geostrophic dynamics, is studied utilizing numerical experiments in an idealized geometry. Finite difference solutions to initial value problems are obtained for a stratified, six-layer fluid in a periodic, flat bottom, f plane channel. The initial flow field in all experiments includes a uniform along-channel jet with horizontal and vertical structure obtained from CTZ hydrographic and current measurements made in May 1987. The maximum velocity in the jet is about 0.5 m s^{-1}, the vertical shear is such that the velocities below 500 m depth are small, and the jet width is about 60 km. The Rossby radius for the first baroclinic mode is 24.6 km. An analysis of the linear stability of the jet flow field in part 1 shows that the jet is linearly unstable to disturbances with along-jet wavelengths greater than 50 km. The largest growth rate is found for a wavelength around 260 km. The objectives here are to find the characteristics of the finite amplitude nonlinear jet instabilities and to examine local dynamical balances for signatures of instability processes that would help with the physical interpretation of results from limited-area CTZ data assimilation models. Experiments are run with periodic channels of different length $L^{(x)}$, where the initial flow includes the basic jet and a small perturbation in the form of the most unstable linear mode for a wavelength equal $L^{(x)}$. In the basic experiment (BC) $L^{(x)}$ = 250 km. One experiment (LC) is run in a long channel $L^{(x)}$ = 1280 km with initial disturbances forced by application of a weak wind stress curl for three days. For times less than about 70 days, experiments BC and LC show the growth and development of finite amplitude meanders in the CTZ jet with spatial variations similar to those observed in spring 1987. During this early time period, the amplitudes of the meanders grow at rates of 1-4 km d^{-1}, increasing with meander amplitude, and the meanders propagate in the direction of the jet upper layer flow at phase velocities of 5-3 km d^{-1}, decreasing with meander amplitude. Initially, at small amplitudes the instability involves comparable contributions from barotropic and baroclinic processes in agreement with linear theory, but for large amplitude meanders the baroclinic energy conversion processes dominate. The vertical velocity field develops a characteristic spatial structure in relation to the jet meanders as do terms in the kinetic energy balance corresponding to the time rate of change of kinetic energy following fluid particles and to the rate of conversion from potential energy. The spatial structure of the latter field may provide a useful indication for jet baroclinic instability processes in limited-area models. At later times in experiment BC (days 90–110), the meander growth is limited by a pinching-off process that results in the formation of detached eddies on both sides of the jet. This process is characterized by a large relative increase of the kinetic energy in the lower layers and in the depth-independent component of the flow. Experiments with $L^{(x)}$ = 180 and 150 km give qualitatively different behavior than that found in experiments BC and LC. The meander growth is bounded, and the jet flow field exhibits time-dependent variations in the volume integrated kinetic and potential energies. For large time the flow may asymptotically approach a nearly steady state or states with irregular or nearly periodic oscillations in the integrated kinetic and potential energies.

1. INTRODUCTION

Hydrographic and Acoustic Doppler Current Profiler (ADCP) measurements of density and horizontal current fields off northern California in the coastal transition zone (CTZ) experiments in spring 1987 [*Kosro et al.*, this issue] and in summer 1988 [*Huyer et al.*, this issue] clearly show the presence of a strong, time-dependent, generally southward flowing jet. The structure of the jet varies in time and space, but it is typically characterized by maximum velocities at the surface of 0.4–0.9 m s^{-1}, vertical shear such that the current velocities below 500 m depth are small, and a horizontal across-jet scale of 60-100 km. An example of the observed jet velocity field is illustrated by the across-jet profiles of along-jet currents at various depths shown in Figure 1. We will refer to this observed jet structure as the CTZ jet.

The origin of the observed jet and the dynamical reasons for its presence are not well understood and are subjects for continuing research. The observed time-dependent behavior [*Kosro et al.*; *Huyer et al.*, this issue] intuitively appears to be consistent with meandering related to finite amplitude flow instability of the basic jet velocity and density fields. Some characteristics of the potential vorticity dynamics and the energetic balances associated with the CTZ jet are revealed in the analysis of the data assimilation, numerical solutions of *Walstad et al.* [this issue]. That study utilizes hydrographic and ADCP data from surveys during May 18–27, and June 9–18, 1987 [*Kosro et al.*, this issue], to construct, by objective analysis, the geostrophic stream function fields in a rectangular region 324 km by 108 km for May 22 and for June 12. The current profiles shown in Figure 1 are calculated at one particular across-jet line, as explained by *Pierce et al.* [this issue] (hereinafter referred

Paper number 91JC00980.
0148-0227/91/91JC-00980$05.00

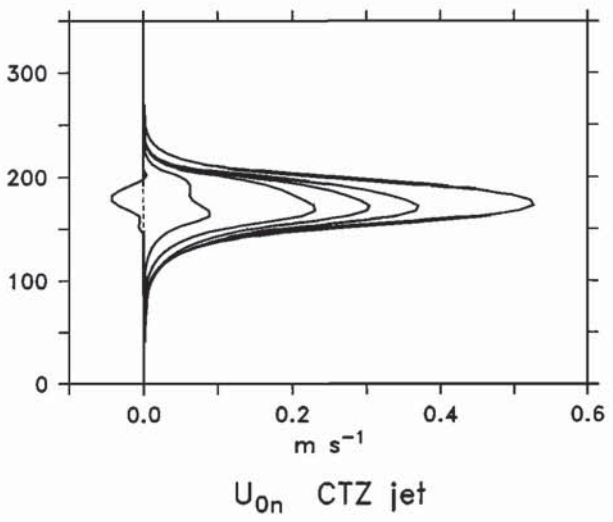

Fig. 1. The velocity field of the CTZ jet utilized in the numerical experiments in Table 2. The x direction velocities U_{0n} for the six layers $n = 1, \ldots, 6$ specified in Table 1 are shown as a function of y in km for $L^{(y)} = 350$ km. The velocities in the near-surface top layer $n = 1$ have the largest values. The maximum velocity magnitudes decrease monotonically for increasing depth. The velocities are found from one across-jet transect in the geostrophic stream function field for May 22, 1987, calculated by *Walstad et al.* [this issue] from the CTZ data of *Kosro et al.* [this issue] as explained in part 1 [*Pierce et al.*, this issue].

to as part 1) from the stream function fields for May 22. *Walstad et al.* [this issue] initialized a quasi-geostrophic numerical model with the stream function field from May 22. The model is then time-stepped forward to June 12 using boundary conditions obtained by linear interpolation between the observed boundary values on May 22 and on June 12. Agreement of the final model-produced stream function for June 12 and the observed field for June 12 is assessed as a function of the parameters used for the objective analysis and for the model implementation. In general, reasonably good agreement is found as documented in detail by *Walstad et al.* [this issue]. The time-dependent potential vorticity and energy balances given by the model are then studied (e.g., as by *Pinardi and Robinson* [1986]) to provide information on the dynamical processes occurring in the ocean in the region of the CTZ field experiment.

During the course of the study by *Walstad et al.* [this issue], it became apparent that being able to quantify the dynamical balances in a particular region of the ocean, where the size of that region is necessarily small because of practical limits on direct observations, is only part of the capability necessary to achieve understanding. The interpretation of the observed balances in terms of identifiable physical processes is also an important component of the study. At the same time, the available information on the local dynamical signatures of finite amplitude, nonlinear flow processes is sparse, and insight into process identification from detailed dynamical balances in limited-area domains over restricted time intervals is not well developed. For example, the question naturally arises of how instability processes in the CTZ jet, if present, are identified from a data assimilation numerical model solution, such as that of *Walstad et al.* [this issue], when the model domain includes only a relatively small part of the jet. Or, more specifically, how do we recognize finite amplitude baroclinic or barotropic instability processes from an examination of local dynamical balances over limited time periods?

In order to help answer the above questions and others like them, we have pursued additional process studies of the dynamics of the CTZ jet. These studies involve jet behavior in idealized situations, but they are based on the observed structure of the jet as found in the CTZ field measurements and as represented in the CTZ data assimilation experiments. In part 1 the linear stability properties of the CTZ jet are examined. Typical observed jet velocity profiles, including those in Figure 1, are assumed for an initially uniform straight jet governed by quasi-geostrophic dynamics. Linear modes of instability are calculated as a function of along-jet wavelength to give information on growth rates, modal structure, and energy balances. In this paper (part 2), we continue the study of CTZ jet instability by examining finite amplitude, nonlinear behavior. The observed CTZ jet profiles in Figure 1 are utilized as initial conditions for a uniform, straight jet aligned along the axis of a periodic f plane channel. The jet structure is perturbed and the subsequent time-dependent, nonlinear adjustment is found from numerical finite difference solutions to the governing quasi-geostrophic potential vorticity equation. The behavior of the jet, as shown by the time variations in the stream function, vertical velocity, vorticity, and potential vorticity fields, is studied. In addition, the contributions of different terms in the kinetic and potential energy balances are calculated and assessed. One objective of the present study is to document and characterize the time-dependent, nonlinear CTZ jet behavior. Another objective is to examine the time and spatial dependence of terms in the potential vorticity and energy equations in an effort to find robust signatures of identifiable physical processes in local balances to help in the dynamical interpretation of the CTZ data assimilation numerical experiments.

Many of the existing oceanographic studies of time-dependent finite amplitude jet behavior have been motivated by applications to the Gulf Stream. Previous relevant investigations include the numerical experiments with quasi-geostrophic two-layer baroclinic jets by *Ikeda* [1981] and *Ikeda and Apel* [1981], the thin-jet model studies of *Flierl and Robinson* [1984], the numerical and theoretical work on frontal jets in an equivalent barotropic model by *Pratt and Stern* [1986] and *Pratt* [1988], the numerical experiments on barotropic β plane jets by *Flierl et al.* [1987], the numerical Gulf Stream simulations with a quasi-geostrophic regional model by *Robinson et al.* [1988] and with a primitive equation regional model by *Spall and Robinson* [1990], and the studies of two-layer quasi-geostrophic jets along vorticity fronts by *Meacham* [1991]. The objective here of using idealized numerical experiments with an initial jet structure extracted from CTZ observations to find signatures of identifiable physical processes in local dynamical balances differs from the primary objectives of the previous work, although local vorticity and energy balances were examined in the Gulf Stream simulations of *Robinson et al.* [1988] and *Spall and Robinson* [1990].

The outline of this paper is as follows. The geometry of the model domain, the governing quasi-geostrophic equations, and the implied quasi-geostrophic energy balance

equations are presented in section 2. The particular parameter values and initial conditions utilized in a set of numerical experiments are discussed in section 3. The results of the experiments are presented in sections 4, 5, and 6. A summary of findings is given in section 7.

2. FORMULATION

We consider motion governed by the quasi-geostrophic approximation in a stratified fluid with N layers of constant density ρ_n and constant undisturbed layer thicknesses H_n, where the subscript $n = 1, 2, \ldots, N$, denotes layer number starting at the surface and increasing with depth. The basic stratification enters the equations through the values of the reduced gravity at the interfaces between layers,

$$g'_{n+\frac{1}{2}} = g(\rho_{n+1} - \rho_n)/\rho_0, \qquad n = 1, 2 \ldots, N-1, \quad (1)$$

where ρ_0 is the constant average density, g is the acceleration of gravity, and the subscript $n+\frac{1}{2}$ denotes a variable defined at the interface between layers n and $n+1$.

The quasi-geostrophic streamfunction for each layer is

$$\psi_n = \psi_n(x, y, t), \qquad n = 1, 2, \ldots, N, \quad (2)$$

with horizontal geostrophic velocity components,

$$u_n = -\psi_{ny}, \quad (3a)$$

$$v_n = \psi_{nx}, \quad (3b)$$

and vorticity,

$$\zeta_n = v_{nx} - u_{ny} = \psi_{nxx} + \psi_{nyy} = \nabla^2 \psi_n, \quad (3c)$$

where (x, y) are horizontal Cartesian coordinates, t is time, subscripts (x, y, t) denote partial differentiation, and $\nabla^2 = \partial^2/\partial x^2 + \partial^2/\partial y^2$ is the horizontal Laplacian operator. In subsequent equations, the range of $n = 1, \ldots, N$ in (2) for variables defined for each layer and the range of $n = 1, \ , N-1$ in (1) for variables defined at interfaces will be implied. The displacements of the interfaces are given by

$$\eta_{n+\frac{1}{2}} = \frac{f_0}{g'_{n+\frac{1}{2}}}(\psi_{n+1} - \psi_n), \quad (4)$$

and the vertical velocities, defined at layer interfaces, are

$$w_{n+\frac{1}{2}} = w_{n+\frac{1}{2}}(x, y, t), \quad (5)$$

where f_0 is the Coriolis parameter.

The fluid is contained in a periodic channel on an f plane with parallel sidewalls at $y = 0$ and $y = L^{(y)}$ and with periodicity assumed for all variables in the x direction over a distance $L^{(x)}$. The upper surface at $z = 0$ is rigid, where z is the vertical coordinate, and the bottom surface at $z = -H_T = -\sum_{n=1}^{N} H_n$ is flat. The flow may be forced by wind stress (divided by ρ_0) with components $\tau^{(x,y)}(x, y, t)$ in the (x, y) directions through an Ekman layer at the top surface with a depth assumed to be small compared to H_1. The surface and bottom boundary conditions give

$$w(z = 0) = w_{\frac{1}{2}} = f_0^{-1} \text{ curl } \tau, \quad (6a)$$

$$w(z = -H_T) = w_{N+\frac{1}{2}} = 0, \quad (6b)$$

where curl $\tau = \tau_x^{(y)} - \tau_y^{(x)}$.

The governing equations are

$$Q_{nt} = -J(\psi_n, Q_n) - A_H \nabla^6 \psi_n + \delta_{n,1} H_1^{-1} \text{ curl } \tau, \quad (7a)$$

where the quasi-geostrophic potential vorticity for each layer is

$$Q_n = \nabla^2 \psi_n + \frac{f_0^2}{H_n}\left[\frac{1}{g'_{n-\frac{1}{2}}}(\psi_{n-1} - \psi_n) - \frac{1}{g'_{n+\frac{1}{2}}}(\psi_n - \psi_{n+1})\right], \quad (7b)$$

the effects of dissipative processes have been represented in the momentum equations by biharmonic friction terms with coefficient A_H, $J(\psi_n, Q_n) = \psi_{nx} Q_{ny} - \psi_{ny} Q_{nx}$ is the Jacobian operator, and $\delta_{n,1}$ is the Kronecker delta. To make (7a) and (7b) valid for $n = 1$ and $n = N$, we arbitrarily define

$$(g'_{\frac{1}{2}})^{-1} = (g'_{N+\frac{1}{2}})^{-1} = 0. \quad (7c)$$

The potential vorticity equations (7) are derived from the quasi-geostrophic vorticity equations,

$$\nabla^2 \psi_{nt} = -J(\psi_n, \nabla^2 \psi_n) + f_0 H_n^{-1}(w_{n-\frac{1}{2}} - w_{n+\frac{1}{2}}) - A_H \nabla^6 \psi_n, \quad (8)$$

which are defined for each layer, and from the quasi-geostrophic density (or interface displacement) equations,

$$(\psi_n - \psi_{n+1})_t = -J(\psi_{n+\frac{1}{2}}, \psi_n - \psi_{n+1}) - g'_{n+\frac{1}{2}} f_0^{-1} w_{n+\frac{1}{2}}, \quad (9a)$$

where

$$\psi_{n+\frac{1}{2}} = (H_n + H_{n+1})^{-1}(H_{n+1}\psi_n + H_n \psi_{n+1}), \quad (9b)$$

which are defined for each interface. Note that (7), (8), and (9) are written in dimensional variables which will be utilized throughout the paper.

Boundary conditions at the sidewalls include

$$\psi_n = C_{0n}(t) \quad \text{at} \quad y = 0, \quad (10a)$$

$$\psi_n = C_{1n}(t) \quad \text{at} \quad y = L^{(y)}, \quad (10b)$$

where C_{0n} and C_{1n} are determined so that integral constraints involving conservation of mass in each layer and the time rate of change of circulation on the boundaries are satisfied [*McWilliams*, 1977]. Sidewall boundary conditions for the friction terms are

$$\nabla^2 \psi_n = \nabla^4 \psi_n = 0 \qquad \text{at} \qquad y = 0, L^{(y)}. \quad (11)$$

The periodicity condition in x is

$$\psi_n(x, y, t) = \psi_n(x + L^{(x)}, y, t). \quad (12)$$

Equations for the depth-integrated kinetic energy (divided by ρ_0) in each layer,

$$K_n = \frac{1}{2} H_n |\nabla \psi_n|^2 = \frac{1}{2} H_n (\psi_{nx}^2 + \psi_{ny}^2), \quad (13)$$

where ∇ is the horizontal gradient operator $(\partial/\partial x, \partial/\partial y)$, are derived by multiplying (8) by $-H_n \psi_n$ as by *Holland* [1978]. Following the notation of *Pinardi and Robinson* [1986], these may be written

$$K_{nt} = \Delta F_{Kn} + \delta f_{\pi n} - b_n + \Delta F_{\pi n} + D_n - \psi_n \delta_{n,1} \text{ curl } \tau, \quad (14)$$

where

$$\Delta F_{Kn} = -J(\psi_n, K_n), \quad (15a)$$

$$\delta f_{\pi n} = -f_0(w_{n-\frac{1}{2}}\psi_{n-\frac{1}{2}} - w_{n+\frac{1}{2}}\psi_{n+\frac{1}{2}}), \quad (15b)$$

$$b_{n+\frac{1}{2}} = -f_0 w_{n+\frac{1}{2}}(\psi_n - \psi_{n+1}), \quad (15c)$$

$$b_n = H_n\left[(H_{n-1} + H_n)^{-1} b_{n-\frac{1}{2}} + (H_n + H_{n+1})^{-1} b_{n+\frac{1}{2}}\right], \quad (15d)$$

$$\Delta F_{\pi n} = H_n \nabla \cdot \left[\psi_n\left(\frac{\partial}{\partial t} - \psi_{ny}\frac{\partial}{\partial x} + \psi_{nx}\frac{\partial}{\partial y}\right)\nabla\psi_n\right], \quad (15e)$$

$$D_n = H_n \psi_n A_H \nabla^6 \psi_n. \quad (15f)$$

In (14), the time rate of change of kinetic energy K_{nt} is balanced by the advection of kinetic energy ΔF_{Kn}, the rates of vertical pressure work $\delta f_{\pi n}$, negative buoyancy work $-b_n$, horizontal pressure work $\Delta F_{\pi n}$, dissipation D_n, and work due to wind stress forcing $-\psi_n \delta_{n,1}$ curl τ.

Similarly, equations for the potential energy (divided by ρ_0) associated with each interface,

$$A_{n+\frac{1}{2}} = \frac{1}{2}\frac{f_0^2}{g'_{n+\frac{1}{2}}}(\psi_n - \psi_{n+1})^2, \quad (16)$$

may be derived by multiplying (9) by $(f_0^2/g'_{n+\frac{1}{2}})(\psi_n - \psi_{n+1})$ and may be written as

$$A_{n+\frac{1}{2}t} = \Delta F_{An+\frac{1}{2}} + b_{n+\frac{1}{2}}, \quad (17)$$

where

$$\Delta F_{An+\frac{1}{2}} = -J(\psi_{n+\frac{1}{2}}, A_{n+\frac{1}{2}}). \quad (18)$$

In (17), the time rate of change of potential energy $A_{n+\frac{1}{2}t}$ is balanced by the advection of potential energy $\Delta F_{An+\frac{1}{2}}$ and the rate of buoyancy work $b_{n+\frac{1}{2}}$.

It will be convenient to use the following notation for the indicated operations for averaging, integration, and summation:

$$\overline{\psi}_n = \frac{1}{L^{(x)}}\int_0^{L^{(x)}} \psi_n \, dx, \quad (19a)$$

$$\langle K_n \rangle = \int_0^{L^{(y)}}\int_0^{L^{(x)}} K_n \, dx \, dy, \quad (19b)$$

$$\{K\} = \sum_{n=1}^{N} \langle K_n \rangle, \quad (19c)$$

$$\{A\} = \sum_{n=1}^{N-1} \langle A_{n+\frac{1}{2}} \rangle. \quad (19d)$$

With curl $\tau = 0$, it follows from (14) and boundary conditions (11) and (12) that

$$\langle K_n \rangle_t = \langle \delta f_{\pi n} \rangle - \langle b_n \rangle + \langle D_n \rangle, \quad (20)$$

and

$$\{K\}_t = -\{b\} + \{D\}. \quad (21)$$

Likewise, from (17) we obtain

$$\langle A_{n+\frac{1}{2}} \rangle_t = \langle b_{n+\frac{1}{2}} \rangle, \quad (22)$$

and

$$\{A\}_t = \{b\}. \quad (23)$$

The sum of (21) and (23) gives

$$[\{K\} + \{A\}]_t = \{D\}. \quad (24)$$

Equation (20) expresses the time rate of change of kinetic energy in each layer $\langle K_n \rangle_t$, due to the net conversion of K_n between layers $\langle \delta f_{\pi n} \rangle$, the conversion of potential to kinetic energy $-\langle b_n \rangle$, and frictional dissipation $\langle D_n \rangle$. The time rate of change of volume-integrated kinetic energy $\{K\}$ is given in (21) by the total potential $\{A\}$ to kinetic $\{K\}$ energy conversion $-\{b\}$ and the total dissipation $\{D\}$. In (22), the time rate of change of $\langle A_{n+\frac{1}{2}} \rangle$ is equal to the potential to kinetic energy conversion term $\langle b_{n+\frac{1}{2}} \rangle$, with a similar interpretation for $\{A\}_t$, in (23). Finally, in (24) the time derivative of the total volume-integrated energy $\{K\} + \{A\}$ is equal to the total dissipation $\{D\}$.

In discussions of the energetic interactions of the unstable CTZ jet in the channel, it will be helpful to utilize also a decomposition of the variables into along-channel, x-averaged quantities (19a) and perturbations about these averages, i.e.,

$$\psi_n(x, y, t) = \overline{\psi}_n(y, t) + \psi'_n(x, y, t). \quad (25)$$

Equations for the area- and volume-integrated kinetic and potential energies associated with the perturbations ψ'_n may be readily derived [e.g., *Pedlosky*, 1987, section 7.2]. Utilizing the definitions,

$$\hat{K}_n = \frac{1}{2}H_n(\psi'^2_{nx} + \psi'^2_{ny}), \quad (26)$$

$$\hat{A}_{n+\frac{1}{2}} = \frac{1}{2}\frac{f_0^2}{g'_{n+\frac{1}{2}}}(\psi'_n - \psi'_{n+1})^2, \quad (27)$$

and again assuming curl $\tau = 0$, we obtain,

$$\langle \hat{K}_n \rangle_t = \langle \delta \hat{f}_{\pi n} \rangle - \langle \hat{b}_n \rangle + \langle KP_n \rangle + \langle \hat{D}_n \rangle, \quad (28)$$

$$\{\hat{K}\}_t = \{KP\} - \{\hat{b}\} + \{\hat{D}\}, \quad (29)$$

$$\langle \hat{A}_{n+\frac{1}{2}} \rangle_t = \langle AP_{n+\frac{1}{2}} \rangle + \langle \hat{b}_{n+\frac{1}{2}} \rangle, \quad (30)$$

$$\{\hat{A}\}_t = \{AP\} + \{\hat{b}\}, \quad (31)$$

$$[\{\hat{K}\} + \{\hat{A}\}]_t = \{KP\} + \{AP\} + \{\hat{D}\}, \quad (32)$$

where

$$\delta \hat{f}_{\pi n} = -f_0(w'_{n-\frac{1}{2}}\psi'_{n-\frac{1}{2}} - w'_{n+\frac{1}{2}}\psi'_{n+\frac{1}{2}}), \quad (33a)$$

$$\hat{b}_{n+\frac{1}{2}} = -f_0 w'_{n+\frac{1}{2}}(\psi'_n - \psi'_{n+1}), \quad (33b)$$

$$\hat{b}_n = H_n\left[(H_{n-1} + H_n)^{-1}\hat{b}_{n-\frac{1}{2}} + (H_n + H_{n+1})^{-1}\hat{b}_{n+\frac{1}{2}}\right], \quad (33c)$$

$$\hat{D}_n = H_n \psi'_n A_H \nabla^6 \psi'_n, \tag{33d}$$

$$KP_n = -H_n \psi'_{nx} \psi'_{ny} \overline{\psi}_{nyy}, \tag{34a}$$

$$AP_{n+\frac{1}{2}} = -\frac{f_0^2}{g'_{n+\frac{1}{2}}} \psi'_{n+\frac{1}{2}x} (\psi'_n - \psi'_{n+1})(\overline{\psi}_n - \overline{\psi}_{n+1})_y. \tag{34b}$$

The interpretation of (28) is similar to that for (20), but in (28) we find an additional term $\langle KP_n \rangle$ representing conversion of kinetic energy from the x-averaged flow to the kinetic energy of the perturbations. Similarly in (30) for $\langle \hat{A}_{n+\frac{1}{2}} \rangle_t$, the term $\langle AP_{n+\frac{1}{2}} \rangle$ represents the conversion of potential energy of the x-averaged flow to the potential energy of the perturbations. In (32) the time rate of change of the volume integrated energy in the perturbations $[\{\hat{K}\} + \{\hat{A}\}]_t$ equals the volume integrals of the production terms $\{KP\}$ and $\{AP\}$ and the dissipation $\{\hat{D}\}$.

We also define kinetic and potential energies associated with the x-averaged flow,

$$\tilde{K}_n = \frac{1}{2} H_n \overline{\psi}^2_{ny}, \tag{35}$$

$$\tilde{A}_{n+\frac{1}{2}} = \frac{1}{2} \frac{f_0^2}{g'_{n+\frac{1}{2}}} (\overline{\psi}_n - \overline{\psi}_{n+1})^2, \tag{36}$$

and note that

$$\{K\} = \{\hat{K}\} + \{\tilde{K}\}, \tag{37}$$

$$\{A\} = \{\hat{A}\} + \{\tilde{A}\}. \tag{38}$$

3. Description of Numerical Experiments

We conduct a set of numerical experiments to study the finite amplitude behavior of the CTZ jet. Numerical solutions to (7) for $\psi_n(x, y, t)$ with boundary conditions from (10), (11), and (12) are obtained for initial value problems in a periodic f plane channel from the finite difference model of *McWilliams* et al. [1978] in the domain

$$0 \le x \le L^{(x)}, \tag{39a}$$

$$0 \le y \le L^{(y)}. \tag{39b}$$

Values of the vertical velocity $w_{n+\frac{1}{2}}$ are obtained from (9a). In addition, to help in the physical interpretation of the results, the terms in the full kinetic (14) and potential energy (17) equations are calculated from finite difference approximations consistent with those used for (7), (8) and (9) and with the derivation of (14) and (17) in difference form. In addition, the decomposition of the variables ψ_n and $w_{n+\frac{1}{2}}$ into x-averaged flow components and perturbations (25) is calculated along with the terms that contribute to the area integrals in the perturbation kinetic (28) and potential (30) energy equations.

In all the experiments we use $f_0 = 9.20 \times 10^{-5} \mathrm{s}^{-1}$, $N = 6$ layers and a total depth $H_T = 3172$ m, with the layer thicknesses H_n and the $g'_{n+\frac{1}{2}}$ values given in Table 1. These values are the same as those used for the basic case linear stability calculations in part 1. They also correspond closely to the parameters used in the data assimilation calculations by *Walstad et al.* [this issue], where the level model equivalents of H_n and $g'_{n+\frac{1}{2}}$ were chosen to resolve the CTZ flow based on the properties of the observed density field in the CTZ experimental region. The Rossby radius of the first baroclinic vertical mode is $\delta_{R1} = 24.6$ km. The experiments are run with various values for $L^{(x)}$ and for $L^{(y)}$. The grid spacing is $\Delta x = \Delta y = 5$ km. Time steps of either 1 hour or 0.5 hour are used. The horizontal biharmonic friction coefficient $A_H = 2 \times 10^8$ m^4 s^{-1} is chosen to be small so that dissipative processes play a nearly negligible role in the time-dependent dynamics of interest.

TABLE 1. Properties Used in the Quasi-Geostrophic Model

Layer n	H_n, m
1	100
2	100
3	100
4	400
5	800
6	1672

Interface $n + \frac{1}{2}$	g', 10^{-2} m s^{-2}
1.5	1.065
2.5	0.337
3.5	0.369
4.5	0.469
5.5	0.395

Total number of layers, N=6. Total depth, $H_T = 3172$ m.

The f plane, periodic, flat bottom channel geometry is utilized so that the finite amplitude behavior of the CTZ jet can be examined as a time-dependent process with no spatial inhomogeneity imposed by topography. We note that the hydrographic and ADCP measurements that defined the presence of the CTZ jet in spring 1987 were, for the most part, located offshore of the continental slope [*Kosro et al.*, this issue]. The CTZ data assimilation study region [*Walstad et al.*, this issue] included only a small part of the outer edge of the continental slope along the inshore boundary of the computational domain. Consequently, the CTZ jet is observed in extensive regions offshore where it is free from direct interaction with the bottom topography of the continental slope. As a result, we feel that a flat bottom is the most appropriate choice for these initial experiments. In addition, the β effect is not included of course in an f plane channel. The observed CTZ jet generally runs north to south, so that the direction of the gradient of f would typically be parallel to the axis of the jet. That geometry is not readily modelled with a periodic channel. The effect of β on the nonlinear instability processes that occur on time scales of 10–60 days, however, should be weak. This is indicated by the very small differences caused by the inclusion of the β effects in the linear stability analysis in part 1; by the small value of the dimensionless parameter $\beta^* = \beta L_H^2 / U_0 \simeq 0.029$ [*Flierl et al.*, 1987], where $\beta = 1.78 \times 10^{-11}$ m^{-1} s^{-1}, $U_0 = 0.55$ m s^{-1} is the approximate maximum velocity in the jet, and $L_H = 30$ km is the approximate jet half width (see part 1); by the relatively large value of the time scale $(\beta \delta_{R1})^{-1} = 26.4$ days; and by the results of the numerical solutions of *Walstad et al.* [this issue], where the β effect was included and was found to play a minor role in the potential vorticity dynamics. The effects of a nonzero gradient in f on the solutions obtained here for longer times are not known.

For all experiments the initial values for the stream function $\psi_n(x,y,0)$ include $\psi_{0n}(y)$, which is defined such that the associated x direction velocity components $U_{0n} = -\psi_{0ny}(y)$ correspond to the CTZ jet velocity profiles shown in Figure 1 and such that $\langle\psi_n(x,y,0)\rangle = 0$. The initial jet is parallel to the x axis and centered in the channel as shown in Figure 1 for $L^{(y)} = 350$ km. The velocity in the top five layers is toward positive x, i.e., $U_{0n} > 0$, for $n = 1-5$. We present results from a set of experiments with different values of $L^{(x)}$ and $L^{(y)}$ where the initial values of ψ_n include, in addition to $\psi_{0n}(y)$, a small perturbation, i.e.,

$$\psi_n(x,y,0) = \psi_{0n}(y) + \psi_{1n}(x,y), \tag{40}$$

where $\psi_{1n}(x,y)$ has the structure of the most unstable linear mode for a wavelength equal to $L^{(x)}$ as found in part 1. The different experiments are summarized in Table 2. In the basic experiment, discussed in section 4, $L^{(x)} = 250$ km which is close to the wavelength of the most unstable linear mode, i.e., to the wavelength where the largest growth rate is found. Some results are discussed also in section 6 for experiments with $L^{(x)} = 150$ and 180 km.

TABLE 2. Summary of Numerical Experiments

Experiment	$L^{(x)}$, km	$L^{(y)}$, km	Amplitude $\psi_{1n}(x,y)$	Initial $\hat{K}/\bar{K}$
BC	250	850	1000	0.0079
LC	1280	650	0	0
180a	180	350	6000	0.334
180b	180	350	2000	0.037
180c	180	350	4000	0.148
150a	150	350	1500	0.025
150b	150	350	4000	0.1788

All of the above experiments were run with $A_H = 2 \times 10^8$ m^4 s^{-1}. The unstable modes are normalized so that the Amplitude $\psi_{1n}(x,y)$ is the maximum absolute value of $\psi_{1n}(x,y)$ in (40). The magnitude of the initial perturbation is also given by Initial $\hat{K}/\bar{K}$ which equals $\{\hat{K}\}/\{\bar{K}\}$ at $t = 1$ day.

To demonstrate the finite amplitude behavior of the CTZ jet when several unstable modes with different along-jet wavelengths may be excited and when the initial conditions are less specialized, in section 5 we present results from one experiment, denoted LC, with $L^{(x)} = 1280$ km and $L^{(y)} = 650$ km. In this case the initial condition is $\psi_n(x,y,0) = \psi_{0n}(y)$. Small disturbances are forced by a weak wind stress curl that is imposed at $t = 0$ for a duration of 3 days and that is then shut off so that it is equal to zero for $t > 3$ days. We use a wind stress of the form

$$\tau^{(x)} = F(t)\cos\left(\frac{\pi y}{L^{(y)}}\right)\sum_{m=1}^{M}\tau_{0m}\ \sin\left(\frac{2m\pi x}{L^{(x)}}\right), \tag{41}$$

where for experiment LC, $M = 9$,

$$\tau_{0m} = (m)^{1/2}\ 2.68 \times 10^{-5}\ \text{m}^2\ \text{s}^{-2}, \tag{42}$$

and

$$F(t) = 1, \qquad 0 \le t \le 2, \tag{43a}$$

$$F(t) = 3 - t, \qquad 2 \le t \le 3, \tag{43b}$$

$$F(t) = 0, \qquad 3 \le t, \tag{43c}$$

where the units of t are days.

4. The Basic Experiment (BC)

The largest growth rates found in part 1 from the linear stability analysis of the CTZ jet profiles in Figure 1 are for along-jet wavelengths of approximately 260 km. In the basic experiment in this section, denoted BC, we examine the finite amplitude behavior of an initial disturbance with a wavelength of 250 km, which is close to the wavelength with maximum linear growth rate. We choose $L^{(x)} = 250$ km and $L^{(y)} = 850$ km and initialize the stream function field as described in (40) with the basic jet structure and with the most unstable linear mode at that wavelength from part 1 (Table 2). The flow is not forced, i.e., curl $\tau \equiv 0$. Equations (7) are integrated forward in time from $t = 0$ to $t = 150$ days.

The finite amplitude behavior of the jet is illustrated by the time-dependent development of the stream function, vorticity, interface displacement, vertical velocity, potential vorticity, and kinetic energy fields. We present results for those fields primarily for layers 1 and 4 because it is in those layers that we generally find the instability processes to be the most active. In Figure 2, contour plots are shown for the (x,y) fields of the variables $\psi_1, \zeta_1/f_0, K_1$, and $w_{1.5}$ every 10 days from 30 to 110 days. The variables $\eta_{1.5}, Q_1$ and $\psi_4, w_{4.5}, Q_4$ are shown in Figures 3 and 4, respectively, for $t = 30$, 50, 70, and 90 days. The (x,y) fields of the terms K_{1t} and ΔF_{K1} from the kinetic energy equation (14) are plotted for the same days in Figure 5. Also included in Figure 5 is a contour plot for layer $n = 1$ of the change in kinetic energy following fluid particles,

$$dK_n/dt = K_{nt} - \Delta F_{Kn}. \tag{44}$$

It follows from (14) with curl $\tau = 0$, that

$$dK_n/dt = \delta f_{\pi n} - b_n + \Delta F_{\pi n} + D_n. \tag{45}$$

Kinetic energy is not conserved on fluid particles, of course, but it changes due to pressure work, conversion to potential energy, and dissipation. Thus, the plots of the dK_n/dt fields show the net effect of those processes which are represented by the terms on the right-hand side of (45). In Figure 6, corresponding plots for layer 4 of $K_4, dK_4/dt$ and $-b_4$ are given, where the potential energy conversion term $-b_4$ is shown specifically to illustrate its contribution in layer 4 to dK_4/dt. The contour plots of fields for the variables from BC in Figures 2–6 are shown for 100 km $< y <$ 750 km, although $L^{(y)} = 850$ km. The nature of the flow at a later time $t = 130$ days is shown by the fields of several variables in Figure 7.

The stream function ψ_1, vorticity ζ_1/f_0, and kinetic energy K_1 fields in Figure 2 clearly show the time-dependent development of the initial linear instability of the jet into finite amplitude meanders that continuously grow in amplitude until about $t = 60$ days when they start to deform and to pinch off to form eddies on either side of the jet. To facilitate the description of the jet, we will refer to that part of the jet meander at small y as the trough and that part at large y as the crest. The location of the eddies that pinch off from the trough (crest) at small (large) y will be referred to as below (above) the jet. The fields at $t = 130$ days (Figure 7) show a weakly meandering jet with a detached, nearly circular, anticyclonic eddy above the jet and a detached, elliptical, cyclonic eddy below the jet. The maximum and minimum values of ζ_n/f_0 in BC, which are similar in magnitude, are plotted as a function of time in Figure 8. The value of

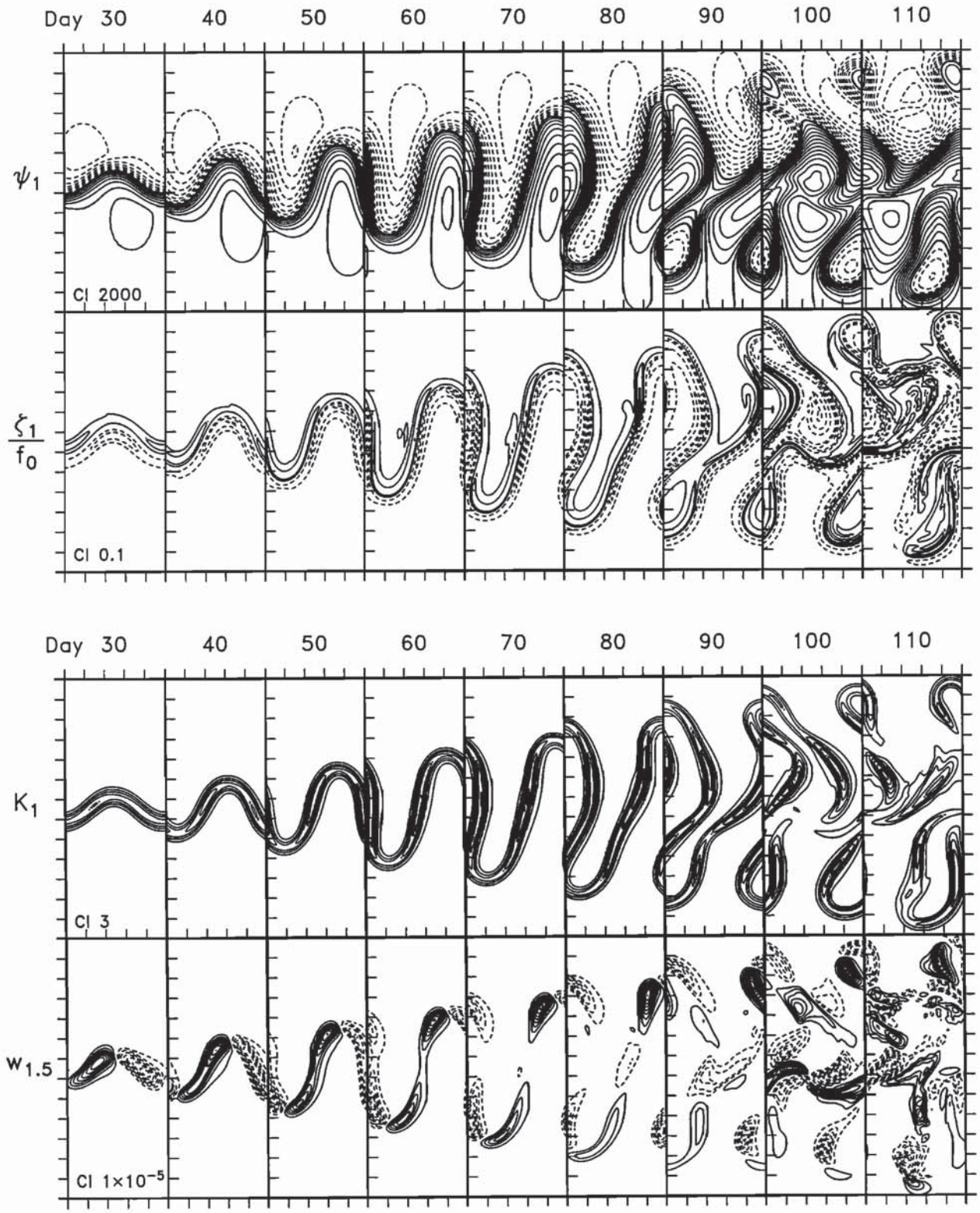

Fig. 2. Contour plots of the $\psi_1, \zeta_1/f_0, K_1$, and $w_{1.5}$ fields as a function of (x, y) every 10 days from $t = 30$ to $t = 110$ days from experiment BC with $L^{(x)} = 250$ km and $L^{(y)} = 850$ km. The fields are shown for $0 \leq x \leq 250$ km and 100 km $\leq y \leq 750$ km. The distance between tick marks on the axes is 50 km. In all contour plots of fields the units are mks. Positive (negative) values are contoured by solid (dashed) lines. In many of the contour plots, the zero contour line is omitted, as for ζ_1/f_0 and $w_{1.5}$ above. When the zero contour line is plotted, as it is for ψ_1, it is represented by a heavy solid line. The contour interval is denoted by CI and applies to all unlabeled panels to the right. When the zero contour line is omitted, 2 CI is the interval between the adjacent solid and dashed lines about the missing zero line.

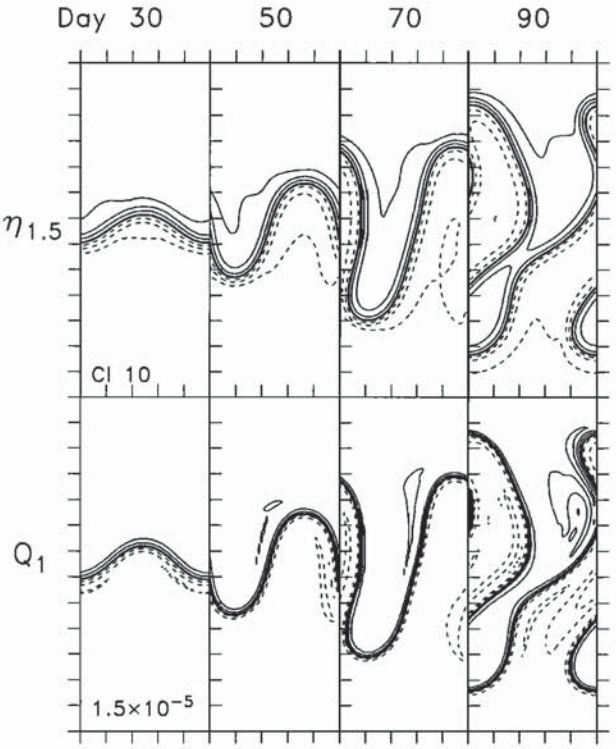

Fig. 3. Contour plots of the $\eta_{1.5}$ and Q_1 fields for days 30, 50, 70, and 90 from experiment BC. Scaling of axes as in Figure 2.

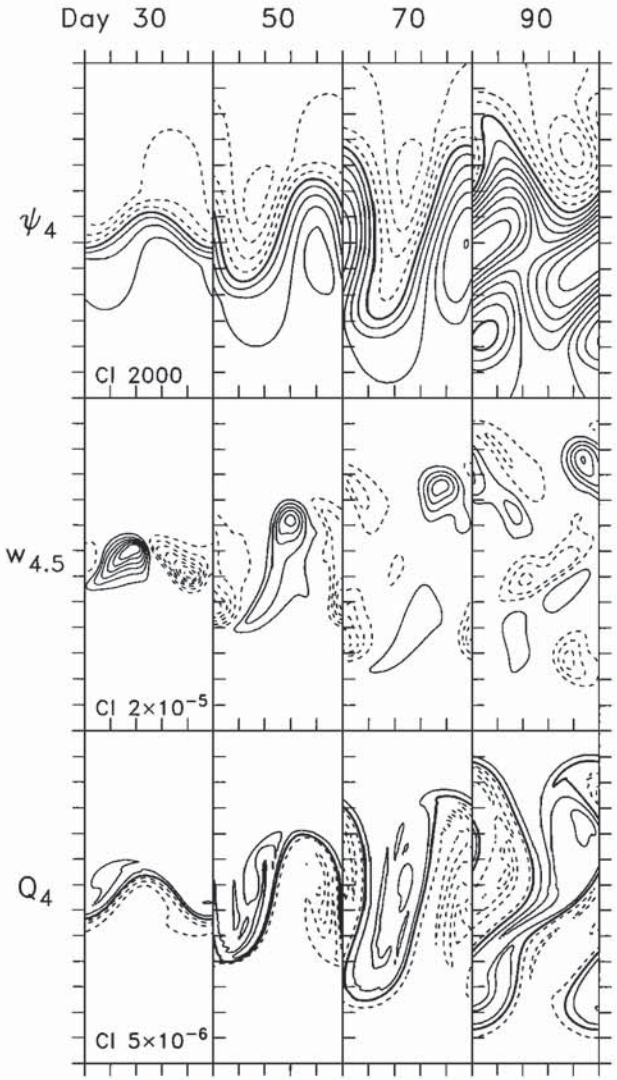

Fig. 4. Contour plots of the $\psi_4, w_{4.5}$, and Q_4 fields for days 30, 50, 70, and 90 from experiment BC. Scaling of axes as in Figure 2.

$|\zeta_n/f_0|_{\max}$ increases gradually from an initial magnitude near 0.2 to a level around 0.3 for $40 \leq t \leq 80$ days. Larger, more variable values around 0.4 are found for $100 < t < 150$ days. The flow therefore is characterized by local Rossby numbers $|\zeta_n/f_0|$ that are less than one, consistent with quasi-geostrophic dynamics, but that are not extremely small. The magnitudes of the meanders in Figure 2 for $t \leq 60$ days correspond generally to those observed in the CTZ jet during the time periods of the spring 1987 CTZ hydrographic and ADCP measurements. Consequently, the nature of the jet behavior and of the dynamical balances in BC for $t \leq 60$ days is of primary concern.

4.1. *Finite Amplitude Meander Development, $t \leq 60$ days*

The propagation velocity of the instability in the x direction is calculated by finding the time variations of the intercepts of the zero stream function line with the initial approximate jet centerline. The phase velocity is toward positive x in the direction of the jet upper layer flow and has a slightly greater magnitude in the crest-to-trough region of the jet. The phase velocity at day 5 has a value of about 4.9 km d^{-1} which is larger than the linear instability result of 4.2 km d^{-1} in part 1. The phase velocity then decreases gradually to 4.2 km d^{-1} at day 25 and to 2.7 km d^{-1} at day 45. Consequently, the movement toward positive x of the crests and troughs of the meanders in the jet that are visible in the ψ_1 fields in Figure 2 directly reflects the phase propagation of the instability. The amplitude of the meanders A_M in the y direction is defined for both the crest and the trough as the absolute value of the displacements in y of the $\psi_1 = 0$ contour from its initial y location. The maximum amplitude occurs initially at the crest and increases from 12.6 km at day 20 to 92.6 km at day 50. Subsequently, it occurs at the trough where it increases from 132.4 km at day 60 to 209 km at day 80. The growth rate of the instability as measured by the time rate of change of the amplitude dA_M/dt is likewise initially greater at the crest, where it increases from about $dA_M/dt = 0.8$ km d^{-1} at day 15 to 2.9 km d^{-1} at day 35. Subsequently at days 45 and 55, the growth rate is larger at the trough where it reaches 4.0 km d^{-1} at day 55. The inverse growth time scale $A_M^{-1} dA_M/dt$, on the other hand, decreases continuously from about 0.089 d^{-1} at day 15 to 0.036 d^{-1} at day 55.

We note first from the $\psi_1, \zeta_1/f_0, K_1$ and Q_1 fields (Figures 2 and 3) that for $t \leq 60$ days as the instability develops, the jet in the top layer retains a coherent structure with relatively small changes in across-jet scale L_{J1}. The corresponding fields in layer 4, e.g., in K_4 (Figure 6), show a decrease in across-jet scale L_{J4} and in the magnitude of the kinetic energy K_4 in the crests and troughs with a general increase in L_{J4} and with larger values of K_4 between the crests and troughs. The general jet structure,

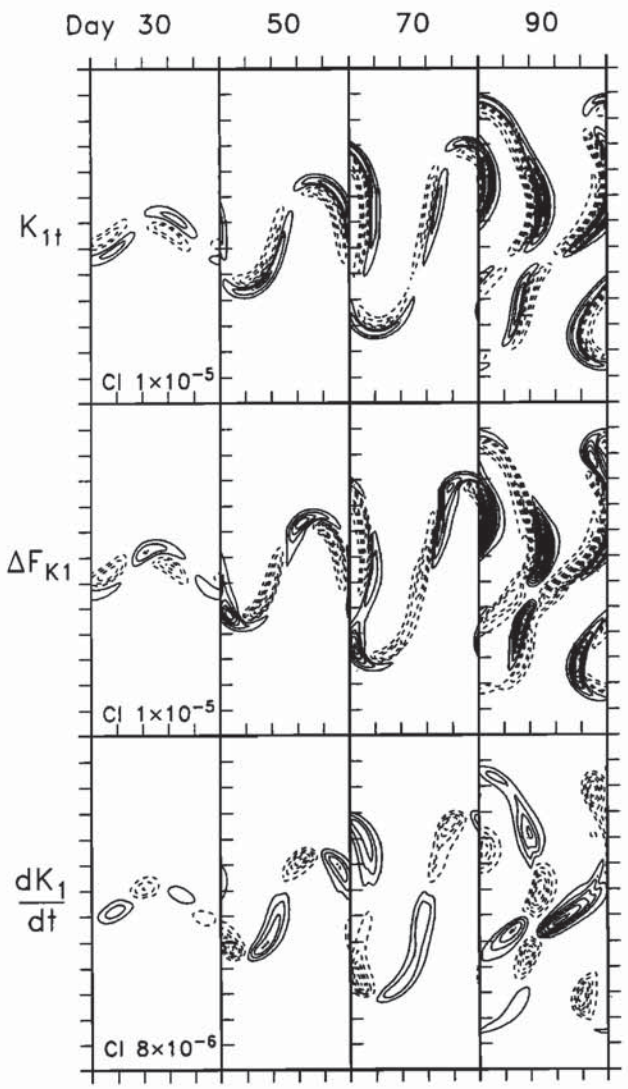

Fig. 5. Contour plots of the $K_{1t}, \Delta F_{K1}$, and dK_1/dt fields for days 30, 50, 70, and 90 from experiment BC. Scaling of axes as in Figure 2.

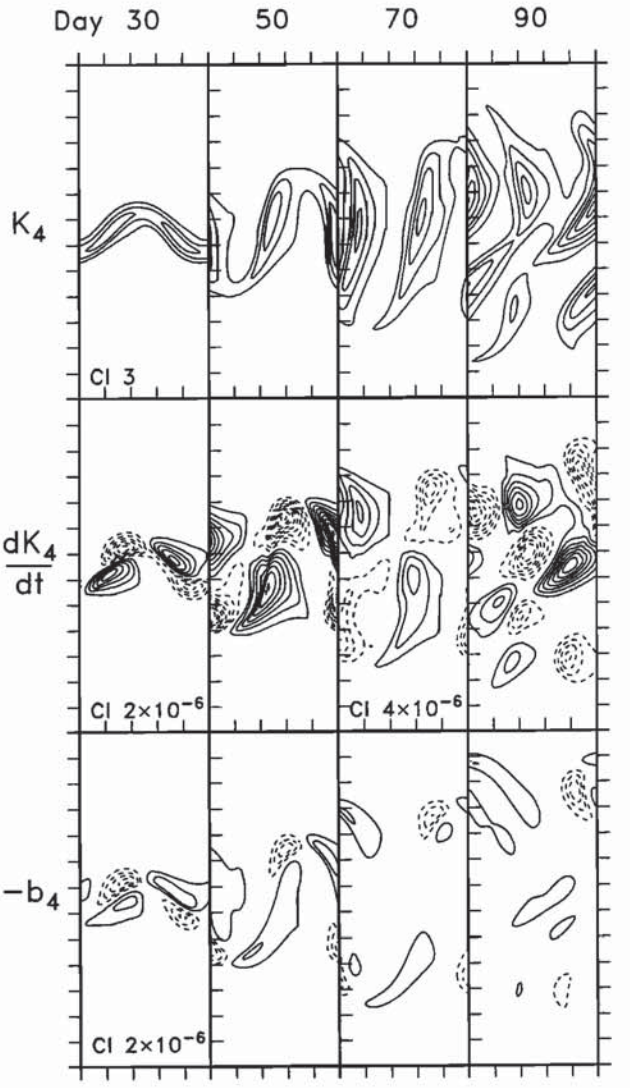

Fig. 6. Contour plots of the $K_4, dK_4/dt$, and $-b_4$ fields for days 30, 50, 70, and 90 from experiment BC. Scaling of axes as in Figure 2.

however, still remains clearly identifiable in layer 4 at day 50. The retention of a strong coherent jet structure near the surface also appears from the measurements [*Kosro et al.*, this issue] to be a feature of the CTZ jet. That property of the observations provides the basic rationale for utilizing particular instantaneous jet profiles for the linear instability analysis in part 1 and for the initial stream function value ψ_{0n} here. The results of the numerical solutions in BC exhibit the same qualitative behavior for $t \leq 60$ days and consequently offer support for that procedure.

The Q_1 potential vorticity field (Figure 3) likewise retains a reasonably coherent structure in the jet similar to the initial values, but for $t = 50$ there is evidence of some shedding of positive Q_1 contours out of the jet behind the crests (i.e., toward negative x). Recall that the initial jet profiles are not symmetric about the centerline. Since Q_1 is nearly conserved on fluid particles (with weak dissipation), this indicates a motion of fluid particles that are initially near the outer edge of the jet away from the jet core as the meanders grow. The vorticity field ζ_1/f_0 shows, as might be expected, an increase in magnitude of negative vorticity in the crests and positive vorticity in the troughs as t increases and as the curvature in the jet increases. The vertical velocity $w_{1.5}$ is positive for fluid particles moving from the troughs to the crests and is negative for particles moving from the crests to the troughs. Since $w_{\frac{1}{2}} = 0$, the $-w_{1.5}$ field also reflects the structure of the vortex stretching term in (8),

$$VS_n = f_0 H_n^{-1}(w_{n-\frac{1}{2}} - w_{n+\frac{1}{2}}), \tag{46}$$

in layer 1. The sign of $w_{1.5}$ and thus of VS_1 is consistent with vorticity ζ_1 decreasing (increasing) for fluid particles entering the crests (troughs). For $t = 20$ (Figure 9), the largest magnitudes of the vertical velocities $w_{1.5}$ are found near the midpoints between the crests and troughs, whereas for later times $t = 30$ to 60 (Figure 2) the maximum magnitudes increase and the largest positive (negative) values of $w_{1.5}$ occur close to the crests (troughs). We point out that from CTZ property distributions in 1988,

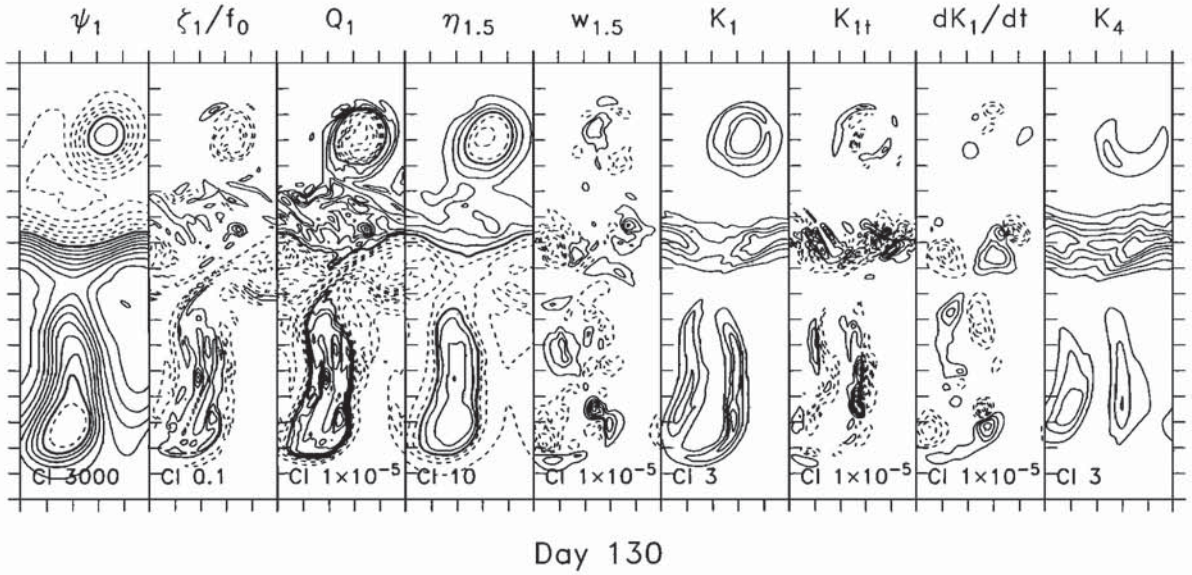

Fig. 7. Contour plots of the $\psi_1, \zeta_1/f_0, Q_1, \eta_{1.5}, w_{1.5}, K_1, K_{1t}, dK_1/dt$, and K_4 fields as a function of (x, y) for day 130 from experiment BC. The fields are shown for $0 \leq x \leq 250$ km and $0 \leq y \leq 850$ km. The distance between tick marks on the axes is 50 km.

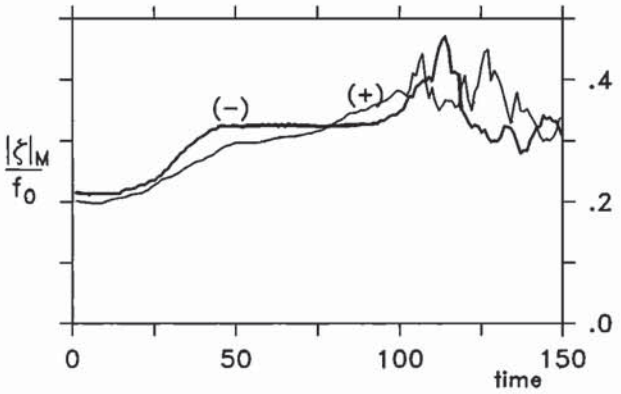

Fig. 8. Time series of the maximum value of ζ_n/f_0 [$|\zeta|_M/f_0$ (+)] and the absolute value of the minimum value of ζ_n/f_0 [$|\zeta|_M/f_0$ (−)] from experiment BC.

Kadko et al. [this issue] and *Washburn et al.* [this issue] have inferred the presence of negative vertical velocities in an offshore-directed part of the CTZ jet. That is consistent with the vertical velocity field $w_{1.5}$ in Figure 2, as the offshore flowing portion of the observed jet corresponds to the crest-to-trough region here. In addition, we note that the along-jet variation of $w_{1.5}$ is qualitatively the same as observed by RAFOS floats in the Gulf Stream [*Bower and Rossby*, 1989]. The displacement fields for the first interface $\eta_{1.5}$ (Figure 3) show a tendency for a concentration of positive (negative) values near the crests (troughs) at days 30 and 50. This evidently reflects a response to the upwelling (downwelling) vertical velocities in the regions ahead of the crests (troughs). Note that the maximum fluctuations in $\eta_{1.5}$ are approximately $\pm$ 30 m which, with $H_1 = H_2 = 100$ m, appears to be consistent, in connection with the validity of quasi-geostrophic dynamics, with the values of $|\zeta_n/f_0|_{\max} \approx 0.3$ in Figure 8.

In layer 4 (Figure 4), the ψ_4 fields exhibit meander patterns very similar to those of ψ_1, but with some spreading of contours near the jet axis as t increases indicating widening of the jet in layer 4. The Q_4 fields show considerable changes from the initial jet structure with shedding and wrapping of positive (negative) Q_4 contours behind the crests (troughs) evidently reflecting erosion of the initial jet structure in layer 4. The vertical velocity $w_{4.5}$ is larger in magnitude than $w_{1.5}$. The vortex stretching term VS_4 (not shown) has a pattern similar to $-w_{4.5}$. For $20 \leq t \leq 50$, the nonzero values of $w_{4.5}$ are not as closely confined to locations near the jet axis as $w_{1.5}$. The greatest positive (negative) values of $w_{4.5}$ for t = 30 and 50 occur for fluid particles just before the crest (trough), similar to $w_{1.5}$.

The K_{1t} fields in Figure 5 are especially useful for indicating the manner in which the jet meanders grow and develop in time. The jet is moving into regions where $K_{1t} > 0$ and out of regions where $K_{1t} < 0$. The progressive movement of the location of the largest positive K_{1t} contours, from a region between the crests and troughs at day 30 to positions closer to the crests and troughs at day 50, illustrates the variation in meander growth characteristics as a function of increasing meander amplitude, i.e., increasing amplitude growth rate and decreasing propagation velocity. The time rate of change of kinetic energy following fluid particles dK_1/dt occurs in an orderly pattern confined to a region along the jet axis in which fluid particles experience increasing K_1 as they accelerate leaving the crests and troughs and decreasing K_1 as they decelerate entering the crests and troughs. This gives dK_1/dt an along-jet variation with a wavelength one-half that of the meanders. In layer 4 (Figure 6), the dK_4/dt field for t = 30 reflects the structure of the potential energy conversion term $-b_4$ with positive values on the lower side of the jet (i.e., toward small y) and negative values on the upper side in the region from trough to crest. The opposite alignment of positive and negative values occurs in the region from crest to trough. For t = 50, the dK_4/dt field has variations in sign along the jet

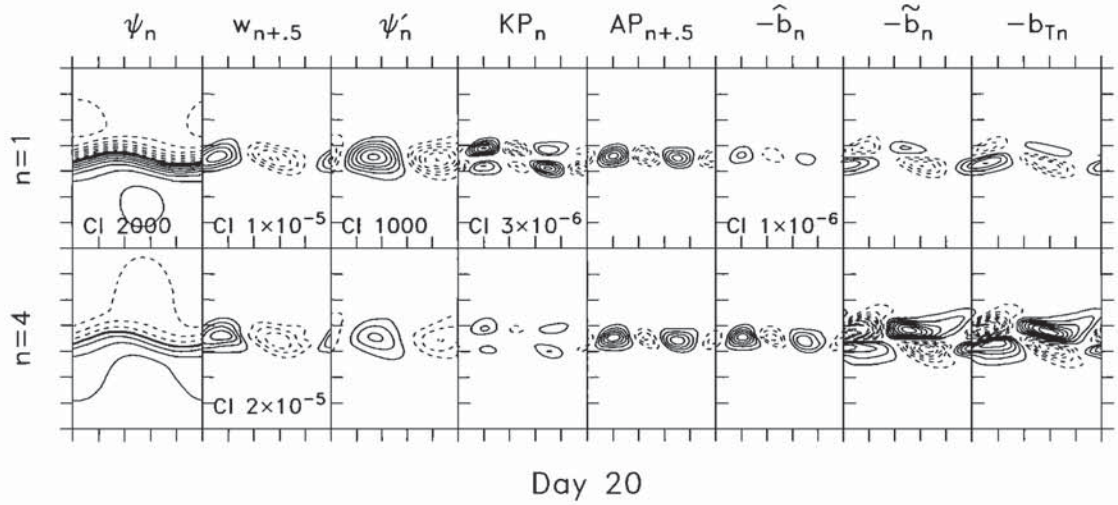

Fig. 9. Contour plots of the $\psi_n, w_{n+\frac{1}{2}}, \psi'_n, KP_n, AP_{n+\frac{1}{2}}, -\hat{b}_n, -\tilde{b}_n$, and $-b_{Tn}$ fields for $n = 1$ and $n = 4$ from day 20 of experiment BC. The fields are shown for $0 \leq x \leq 250$ km and 250 km $\leq y \leq 600$ km. The distance between tick marks on the axes is 50 km. The contour interval CI for $n = 1$ applies to unlabeled panels below for $n = 4$. Fig. 10. Time variation of the volume integrated energy and energy conversion terms from experiment BC. For ease in plotting, the variables have been scaled by $C = (L^{(x)}\, L^{(y)})^{-1}$ and the brackets have been omitted so that the energy terms $K = C\{K\}, A = C\{A\}, \hat{K} = C\{\hat{K}\}, \hat{A} = C\{\hat{A}\}, \tilde{K} = C\{\tilde{K}\}, \tilde{A} = C\{\tilde{A}\}$, and the energy conversion terms $AP = D\{AP\}, KP = D\{KP\}, -b = -D\{b\}$ where $D = 10^6 C$. The potential energies A and $\tilde{A}$ have been displaced by an arbitrary constant reference value for convenience in plotting.

similar to dK_1/dt, but the nonzero values of dK_4/dt are spread over a region of greater extent about the jet axis. This is consistent with the widening of the jet in layer 4 found in the $\psi_4, w_{4.5}$, and K_4 fields. For $t = 50$, the conversion term $-b_4$ is positive along much of the jet, with small regions of relatively large negative values just ahead of the crests and troughs. Note that although the potential energy conversion term $-b_n$ involves the vertical velocities $w_{n+\frac{1}{2}}$, there is no obvious way to infer the structure of the $-b_4$ fields from the $w_{4.5}$ fields alone.

We examine the fields of the perturbation stream function ψ'_n (25) and the energy production terms KP_n and $AP_{n+\frac{1}{2}}$ (34*a*,*b*) for layers 1 and 4 at day 20. These are shown in Figure 9, along with the fields of other variables defined below. The spatial variability of these terms is qualitatively similar to that given by the linear stability analysis in part 1. The structure of ψ'_1 and of ψ'_4 is similar, with stronger fluctuations in ψ'_1. The direction of the implied perturbation velocity is consistent with the jet meander pattern in ψ_1 and ψ_4 at $t = 20$ (Figure 9). The dominance of positive values of KP_1 and of $AP_{4.5}$ is clear. The along-jet wavelength of these fields is one-half that of the basic meander with positive values located just before the crests and troughs.

The time variation of the volume integrated kinetic and potential energies, $\{K\}, \{\hat{K}\}, \{\tilde{K}\}, \{A\}, \{\hat{A}\}, \{\tilde{A}\}$ and the total energy $\{K\} + \{A\}$ are shown for $0 \leq t \leq 150$ days in Figure 10 (where the magnitudes are rescaled and the brackets are omitted). As t increases, the total energy $\{K\} + \{A\}$ decreases slowly due to dissipation. The total kinetic energy $\{K\}$ increases, while the total potential energy $\{A\}$ decreases as the jet instabilities develop. For $t \leq 50$ days, the kinetic and potential energies associated with the x-averaged flow, $\{\tilde{K}\}$ and $\{\tilde{A}\}$, decrease while the kinetic and potential energy in the perturbations, $\{\hat{K}\}$ and $\{\hat{A}\}$, increase.

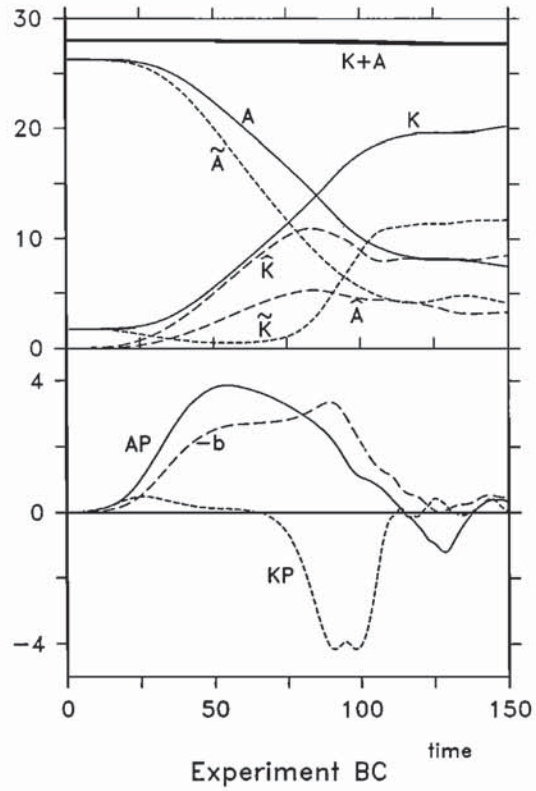

Fig. 10. Time variation of the volume integrated energy and energy conversion terms from experiment BC. For ease in plotting, the variables have been scaled by $C = (L^{(x)}\, L^{(y)})^{-1}$ and the brackets have been omitted so that the energy terms $K = C\{K\}, A = C\{A\}, \hat{K} = C\{\hat{K}\}, \hat{A} = C\{\hat{A}\}, \tilde{K} = C\{\tilde{K}\}, \tilde{A} = C\{\tilde{A}\}$, and the energy conversion terms $AP = D\{AP\}, KP = D\{KP\}, -b = -D\{b\}$ where $D = 10^6 C$. The potential energies A and $\tilde{A}$ have been displaced by an arbitrary constant reference value for convenience in plotting.

The time variation of the volume integrated energy conversion terms $-\{b\}$, $\{KP\}$, and $\{AP\}$ are also shown in Figure 10. The integrated rate of conversion from potential to kinetic energy $-\{b\}$ is positive and, for $t \leq 50$, increases as time increases. The integrated conversion terms $\{KP\}$ and $\{AP\}$ are both positive for $t \leq 50$ and start with nearly equal magnitudes. This indicates that initially the energy conversion term $\{KP\}$ related to horizontal shear and contributing in (29) to an increase in $\{\hat{K}\}$ (referred to as a barotropic instability process), is equal in size to the baroclinic conversion process represented by $\{AP\}$ and contributing in (31) to an increase in $\{\hat{A}\}$. This is consistent with results of the linear stability analysis in part 1. At $t \approx 15$, however, $\{AP\}$ starts to increase relative to $\{KP\}$. This gives one indication that by time $t \approx 15$ the linear solution has started to lose validity. At later times $30 \leq t \leq 70$, $\{AP\}$ is substantially greater than $\{KP\}$ and the energy conversions contributing to growth of total energy $\{\hat{K}\} + \{\hat{A}\}$ in the perturbations in (32) are dominated by the baroclinic processes in $\{AP\}$. Note that for $t \leq 50$ the time variations of the total potential to kinetic energy conversion term $-\{b\}$ is very similar to that of $\{AP\}$.

The contributions from the individual layers or interfaces to $\{K\}$ and $\{A\}$, i.e., $\langle K_n \rangle, \langle \hat{K}_n \rangle, \langle \tilde{K}_n \rangle$, and $\langle A_{n+\frac{1}{2}} \rangle, \langle \hat{A}_{n+\frac{1}{2}} \rangle, \langle \tilde{A}_{n+\frac{1}{2}} \rangle$ are plotted as a function of time in Figure 11. The largest increase in $\langle \hat{K}_n \rangle$ occurs for the bottom layer $n = 6$ with substantial increases also for $n = 1, 4$ and 5. The largest increase in $\langle \hat{A}_{n+\frac{1}{2}} \rangle$ occur for the first and the fourth interfaces $n = 1$ and 4.

The contributions from individual layers or interfaces to $\{KP\}$, $\{AP\}$ and $-\{b\}$, i.e., $\langle KP_n \rangle, \langle AP_{n+\frac{1}{2}} \rangle$, and $-\langle b_n \rangle$, are plotted in Figure 12 and show that for $t \leq 50$ days the largest values of $\langle KP_n \rangle$ occur in layers 1 and 4, while the largest values of $\langle AP_{n+\frac{1}{2}} \rangle$ are from the deeper interfaces 4.5 and 5.5. The largest values of $-\langle b_n \rangle$ are found in layers 4, 5, and 6. Also included in Figure 12 is a plot of $\langle \delta f_{\pi n} \rangle$ which is positive for $n = 1$, 6 and negative for $n = 2$, 3, 4, 5 (recall $\{\delta f_\pi\} = 0$). The largest positive values are for $n = 6$ and the largest negative values for $n = 5$. For short time $t \leq 15$, the relative ordering of $\langle \delta f_{\pi n} \rangle$ (not visible in Figure 12) remains the same and agrees with the prediction of linear theory in part 1. It is primarily the above results that motivate our concentration on layers 1 and 4 to illustrate the spatial variability of the fields.

In data assimilation applications with regional open ocean models, such as that by *Walstad et al.* [this issue], it is generally not feasible to use decompositions such as (25) into spatial- or time-averaged quantities plus perturbations. Thus, employment of energy equations for perturbations, such as (29), (31), and (32), and subsequent physical interpretations for energy conversions between perturbation and averaged fields are usually not possible. The spatial fields of terms in the full kinetic and potential

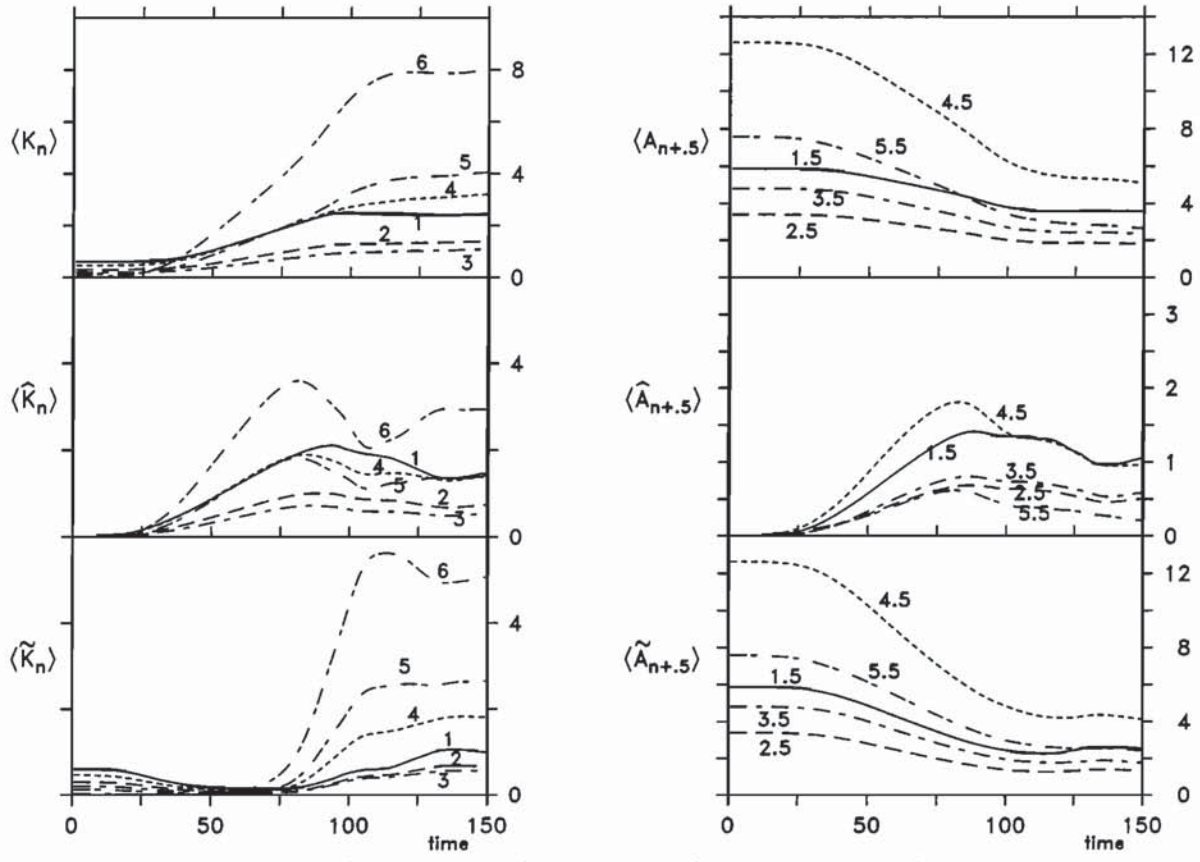

Fig. 11. Time variation of the integrated kinetic energies for each layer and of the integrated potential energies for each interface from experiment BC. The variables have been rescaled so that in the plots $\langle K_n \rangle, \langle \hat{K}_n \rangle, \langle \tilde{K}_n \rangle, \langle A_{n+\frac{1}{2}} \rangle, \langle \hat{A}_{n+\frac{1}{2}} \rangle, \langle \tilde{A}_{n+\frac{1}{2}} \rangle$ represent $C[\langle K_n \rangle, \langle \hat{K}_n \rangle, \langle \tilde{K}_n \rangle, \langle A_{n+\frac{1}{2}} \rangle, \langle \hat{A}_{n+\frac{1}{2}} \rangle, \langle \tilde{A}_{n+\frac{1}{2}} \rangle]$, respectively, where $C = (L^{(x)} L^{(y)})^{-1}$ consistent with Figure 10.

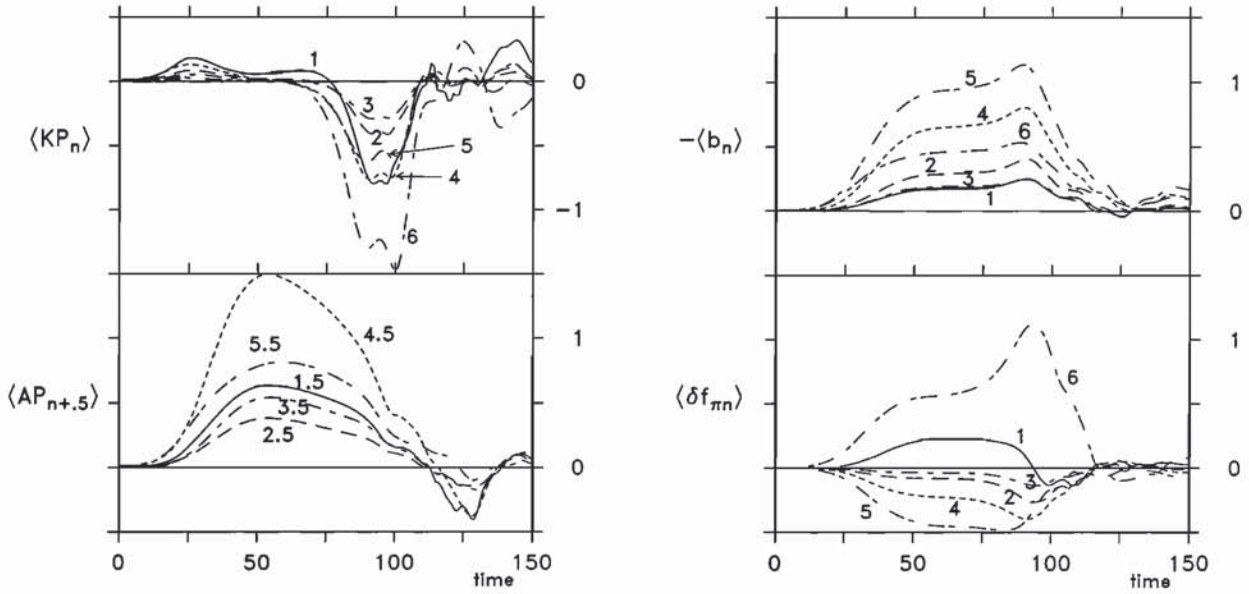

Fig. 12. Time variation of the integrated energy conversion terms for each layer or each interface from experiment BC. The variables have been rescaled consistent with Figure 10 so that in the plots $\langle KP_n\rangle, \langle AP_{n+\frac{1}{2}}\rangle, -\langle b_n\rangle, \langle \delta f_{\pi n}\rangle$ represent $D[\langle KP_n\rangle, \langle AP_{n+\frac{1}{2}}\rangle, -\langle b_n\rangle, \langle \delta f_{\pi n}\rangle]$, respectively, where $D = 10^6 C$ and $C = (L^{(x)}L^{(y)})^{-1}$.

energy equations (14) and (17) are accessible, however, and may be examined as by *Pinardi and Robinson* [1986]. The objective is to try and find a way to interpret the behavior of those terms to shed light on the underlying dynamical processes in a manner similar to that possible with $\{KP\}$ and $\{AP\}$ for energy conversions between averaged quantities and perturbations.

The energy conversion terms KP_n and $AP_{n+\frac{1}{2}}$ originate in the advection terms ΔF_{Kn} in (14) and $\Delta F_{An+\frac{1}{2}}$ in (17), respectively, but generally have $\langle KP_n\rangle \neq 0$, $\langle AP_{n+\frac{1}{2}}\rangle \neq 0$, whereas $\langle \Delta F_{Kn}\rangle = 0$ and $\langle \Delta F_{An+\frac{1}{2}}\rangle = 0$. Consequently, there is little hope for seeing signatures of KP_n or $AP_{n+\frac{1}{2}}$ in ΔF_{Kn} or in $\Delta F_{An+\frac{1}{2}}$. On the other hand, the results in Figures 10 and 12 show that for $t \leq 50$ days the time variability of $-\{b\}$, representing the net conversion from potential to kinetic energy, is closely related to that of $\{AP\}$. Since $\langle b_n\rangle \neq 0$, one possibility for identifying baroclinic conversion processes in the CTZ jet may be provided by an examination of the $-b_n$ fields in the kinetic energy equation (14).

We examine that possibility further by looking at contour plots of the $-\hat{b}_n, -\tilde{b}_n$ and $-b_{Tn}$ fields for day 20 (Figure 9), where $\hat{b}_n$ is defined in (33*b*) and (33*c*) and

$$\tilde{b}_{n+\frac{1}{2}} = -f_0 w'_{n+\frac{1}{2}}(\overline{\psi}_n - \overline{\psi}_{n+1}), \tag{47a}$$

$$\tilde{b}_n = H_n\Big[(H_{n-1}+H_n)^{-1}\tilde{b}_{n-\frac{1}{2}} + (H_n + H_{n+1})^{-1}\tilde{b}_{n+\frac{1}{2}}\Big], \tag{47b}$$

$$b_{Tn} = \hat{b}_n + \tilde{b}_n, \tag{48}$$

$$\langle b_{Tn}\rangle = \langle \hat{b}_n\rangle, \tag{49a}$$

$$\langle \tilde{b}_n\rangle = 0. \tag{49b}$$

We find from the solutions that $w'_{n+\frac{1}{2}} \simeq w_{n+\frac{1}{2}}$. This implies that $b_{Tn} \simeq b_n$ which is substantiated by a comparison of the $-b_{T4}$ field in Figure 9 with the $-b_4$ field for day 20 (not shown). The dominance of positive values in $-\hat{b}_4$ and the similarity in structure of the $-\hat{b}_4$ field to the $AP_{4.5}$ field are evident. The $-b_{T4}$ field (or, equivalently, the $-b_4$ field) contains in addition to $-\hat{b}_4$ substantial contributions from $-\tilde{b}_4$, which in fact has zero area average (49*b*). One general task with limited area models then is to identify the net positive contributions produced by $-\hat{b}_4$ from an inspection of a typically incomplete picture of the $-b_4$ field. From Figure 9, it appears that for day 20 that is not readily accomplished. For larger times, however (e.g., at $t = 30$ and $t = 50$ (Figure 6)), it is possible to see the dominance of positive values in the $-b_4$ fields. The locations of the regions where $-b_4$ is negative, ahead of and close to the crests and troughs, are also clearly indicated. Consequently, the structure of the fields of the conversion terms $-b_n$ may provide insight into the occurrence of baroclinic instability processes in limited-area data assimilation models that contain only part of the CTZ jet.

We note that, in addition to the kinetic energy balance terms plotted in Figures 5 and 6, we examined the spatial fields of all the individual terms in the kinetic energy equation (14) and also the terms in the potential energy (17) and the potential vorticity (7) equations. Other than the fact that the $b_{n+\frac{1}{2}}$ fields in (17) were similar in structure to the b_n fields in (14), we found the clearest signatures of the jet behavior for $t < 60$ days in the fields presented in Figures 2–6.

4.2. *Detachment of Eddies, $t > 60$ days*

At $t = 60$ days the $\psi_1, \zeta_1/f_0$, and K_1 fields in Figure 2 show a visible small distortion in the growth and propagation of the meander pattern reflecting an apparent lag toward small x of the trough. This tendency of the

trough meander to lean backward is accentuated at day 70. By day 80, the trough loop has started to pinch off. The pinching-off process continues through days 90 and 100 such that by day 110 a cyclonic elliptical eddy has essentially detached below the jet. During the period between days 90 and 100, a smaller, more nearly circular, anticyclonic eddy starts to pinch off and by day 110 begins to detach from the crest above the jet. It may be seen from the K_1 (Figure 2) and the K_{1t} (Figure 5) fields that the pinching-off process proceeds differently at the trough and at the crest. For the meander loop forming the trough, the K_{1t} fields (Figure 5) show that the leading part of the trough meander changes its relative movement, that at days 50 and 70 is forward (i.e., downstream toward positive x), so that by day 90 it is moving backward toward the trailing part of the loop, which is likewise moving backward. The backward movement at the leading portion closes the separation between the leading and trailing edges most strongly at a distance of about 250 km from the extremity of the trough, and this ultimately results in the pinching off of an elliptic cyclonic eddy. The detachment process at the crest, on the other hand, appears to result primarily from a faster relative movement forward of the trailing part of the meander loop such that it overtakes the leading part, which is also moving forward. The pinching-off process occurs at about 150 km distance from the tip of the crest and a nearly circular, anticyclonic eddy is detached.

Later, at day 130 the K_1 field (Figure 7) clearly shows the presence of a jet with a very weak meander that is roughly twice as wide ($L_{J1} \simeq 100$ km) as the original jet (compare with the K_1 field at day 30 in Figure 2 where $L_{J1} \simeq 60$ km) but with similar K_1 magnitudes. The K_1 field at day 130 also clearly shows that the nearly circular anticyclonic eddy above the jet has a diameter of about 150 km, while the elliptical cyclonic eddy below the jet has a minor axis (aligned along the jet) of approximately 150 km and a major axis (normal to the jet) of about 325 km.

The integrated energy and energy conversion terms exhibit a change in behavior starting about $t \simeq 50$ days near the beginning of the eddy detachment process. The first indications of change occur in $\{AP\}$ and $-\{b\}$ (Figure 10) at about day 50 when $\{AP\}$ stops increasing and starts decreasing and when $-\{b\}$ stops increasing and levels off. The variation in $\{AP\}$ primarily reflects a similar variation in $\langle AP_{4.5}\rangle$ (Figure 12). The general increase of $\{K\}, \{\hat{K}\}$, and $\{\hat{A}\}$ and the corresponding decrease of $\{A\}, \{\tilde{A}\}$, and $\{\tilde{K}\}$ that begins about $t = 30$ (Figure 10) continues, however, to approximately $t = 70$ days. At that time, $\{\tilde{K}\}$ starts to increase rapidly until about day 110. This increase is evidently in response to a sharp decrease near $t = 70$ of the kinetic energy conversion term $\{KP\}$ to relatively large negative values. The variation of $\{KP\}$ is due to corresponding variations in $\langle KP_n\rangle$ primarily for the bottom layer $n = 6$, but also for $n = 1$, 4, and 5. The time period $70 \leq t \leq 110$ of the rapid increase in $\{\tilde{K}\}$ corresponds to that during which the meanders pinch off at the trough and crest to form detached eddies. The increase of $\{\tilde{K}\}$ primarily occurs through increases in $\langle \tilde{K}_n\rangle$ for the bottom layer $n = 6$ and, to a lesser extent, for the lower layers $n = 5$ and 4 (Figure 11). Accompanying the increase in $\{\tilde{K}\}$ is a leveling off and decrease in $\{\hat{K}\}$ from $t = 80$ to 110, due mainly to a decrease in $\langle \hat{K}_6\rangle$. The changes in $\{\tilde{K}\}$ and $\{\hat{K}\}$ are such that the total kinetic energy $\{K\}$ increases steadily from about $t = 50$ to 100, mainly reflecting an increase in the kinetic energy in the bottom layer $\langle K_6\rangle$. During the time $75 \leq t \leq 110$, the conversion term $\langle \delta f_{\pi 6}\rangle$ is large and positive and thus a primary source, along with a somewhat smaller $-\langle b_6\rangle$, for the increase of $\langle K_6\rangle$. After about $t = 110$, corresponding to the completion of the major part of the pinching-off process, the energy conversion terms (Figures 10 and 12) generally collapse to much smaller values and the integrated energy terms (Figures 10 and 11) level off. As a consequence, the eddy detachment process results for $t > 120$ days in significantly increased values of kinetic energy in the bottom layer $\langle K_6\rangle$, associated with increases in both $\langle \tilde{K}_6\rangle$ and $\langle \hat{K}_6\rangle$. Similar increases, but with smaller magnitudes occur for the kinetic energies in layers 5 and 4. The increase of $\langle K_4\rangle$ is illustrated by a comparison of the K_4 fields at day 30 (Figure 6) and at day 130 (Figure 7). Thus the jet at day 130 is not only wider than the original jet, but it has significantly greater relative amounts of kinetic energy in the deeper layers. We note that similar qualitative variations with time of integrated energy and energy conversion terms were found during eddy detachment in the two-layer, quasi-geostrophic, β plane jet instability studies of *Ikeda* [1981].

A different and illuminating representation of the meander pinch-off and eddy detachment process is given by the time variation of the x-averaged velocity profiles $\overline{u}_n(y,t)$ in Figure 13. At day 30, the $\overline{u}_n$ profiles still represent a jet centered in the channel, but with magnitudes reduced from the initial values in agreement with the decrease in $\{\tilde{K}\}$ in Figure 10. The growth of the meander amplitudes is such that by days 50 and 70 the x-averaged velocities have distinct peaks near the y locations of the crest and the trough. By day 90, a positive jet flow and somewhat weaker counterflow that are notably almost depth-independent have developed between the vertically sheared peaks at the outer edges. The central jet structure in $\overline{u}_n$ continues to increase in strength during days 110 to 130. By day 130, the central jet has developed some vertical shear but retains a large magnitude depth-independent component. The presence of the anticyclonic, nearly circular eddy above the jet at day 130 is visible in the $\overline{u}_n$ profiles which indicate substantial vertical shears in this eddy. The elliptic cyclonic eddy below the jet, on the other hand, results in a signature in $\overline{u}_n$ that involves vertical shear for the positive velocities at small y but nearly depth-independent negative velocities at larger y. This is consistent with the structure of the elliptic eddy given by the K_1 and K_4 fields at day 130 in Figure 7, which show small magnitudes for K_1 and K_4 at the part of the eddy near the jet at large y and larger K_1 with small K_4 at the opposite side near small y. The significant increase in $\{\tilde{K}\}$ for the x-averaged flow from day 70 to day 110 during the eddy detachment process is clearly visible in the $\overline{u}_n$ profiles in Figure 13. Also, obvious is the major growth in $\langle \tilde{K}_n\rangle$ for the deeper layers $n = 5$ and 6 and the resultant large increase in the depth-independent, barotropic component of the flow.

The vertical velocity fields $w_{1.5}$ and $w_{4.5}$ (Figures 2 and 4) at day 70 generally appear to represent a continuous development from day 50, with further concentration near the crests and troughs of positive (negative) values

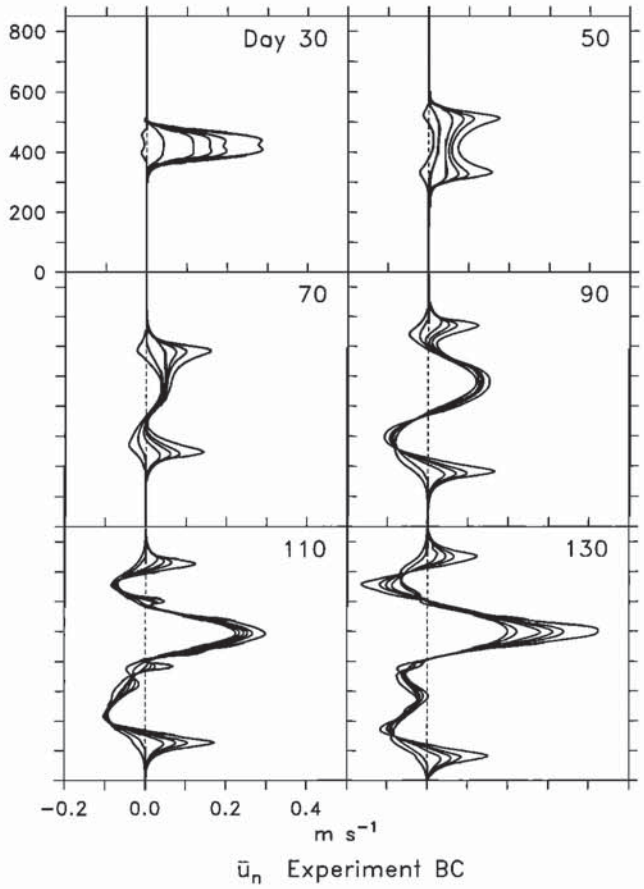

Fig. 13. The x-averaged velocities $\bar{u}_n$ as a function of y in km for days 30, 50, 70, 90, 110, and 130 from experiment BC. The maximum absolute values of the velocities generally decrease monotonically with depth.

for particles entering the crests (troughs) and negative (positive) values for particles leaving the crests (troughs). For day 90, however, the $w_{1.5}$ and $w_{4.5}$ fields show increased structure with, most notably, an additional region of negative values in the central part of the field near the location of the trough pinch-off point. These negative values of $w_{1.5}$ presumably contribute through the vortex stretching term (46) in (8) to the positive vorticity region behind the trailing loop of the crest meander, visible in the ζ_1/f_0 fields for days 90 and 100 in Figure 2. The ζ_1/f_0 field (Figure 2) shows nicely the pinching off of the trough meander loop at day 90 and of the crest loop around day 110. The development of small-scale structures in the ζ_1/f_0 field by day 110 is also evident. For days 100 to 110, the $w_{1.5}$ field develops increasingly complex structure in both the detaching eddies and in the central jet region. The change in the $w_{1.5}$ field is tied, through the vortex stretching term (46), to the strong evolution of the vorticity field ζ_1/f_0 during the eddy detachment process. It becomes difficult during this period, because of the increasing complexity of the flow, to characterize the physical process in terms of local variations in $w_{1.5}$ and ζ_1/f_0.

The dK_1/dt fields (Figure 5) change structure from day 70 to day 90 and at day 90 show a decrease in K_1 for particles approaching the location of the pinch-off point along both the crest and the trough sides of the meander loop and an increase of K_1 for particles leaving the location of that point. The dK_4/dt fields (Figure 6) for days 70 and 90 have patterns very similar to those of dK_1/dt but spread over a greater region and not confined as closely to the location of the jet axis. The magnitude of the variations in the dK_4/dt field increases markedly around day 90 (note the contour interval). In addition, $-b_4$ (Figure 6) clearly plays a much smaller role in the local dK_4/dt balance in (45) for days 70 and 90 than it does earlier at t= 30 and 50, although the integrated contribution $-\langle b_4 \rangle$ to $\langle K_4 \rangle_t$ in (20) remains appreciable and greater in magnitude than $\langle \delta f_{\pi 4} \rangle$ through $t = 100$ (Figure 12). This latter behavior, where large local variations in terms obscure net integrated effects, illustrates some of the difficulty associated with efforts to identify processes from local dynamical balances in situations where the flow is strongly evolving in a complex manner.

The presence of extensive small-scale variations in the ζ_1/f_0 and Q_1 fields later at day 130 may be clearly seen in Figure 7. Note that at day 130, the nearly circular anticyclonic eddy above the jet has negative values of Q_1 in its core while the elliptical cyclonic eddy below the jet has positive Q_1 core values reflecting, as is typical for jet eddy detachment processes, the transport of fluid across the jet from initial locations (Figure 3). The vertical velocity field $w_{1.5}$ at $t = 130$ likewise is characterized by extensive small-scale structure although, similar to the $w_{1.5}$ pattern for $t \leq 70$, there are still generally negative values in the jet upstream of the weak trough and positive values downstream. In contrast to the situation for $t \leq 90$ days, the dominant time-dependent evolution of the flow at day 130 is not clearly indicated by the K_{1t} field which also contains a great deal of small-scale structure. The dK_1/dt field shows a little more order than K_{1t}, with behavior similar to that found for $t \leq 90$ days in that dK_1/dt is negative in the jet for particles entering the trough and crest and positive for particles leaving the trough. The same general pattern is visible in the elliptic eddy near the top and bottom points of greatest curvature.

In general, the small-scale variability and scarcity of clear dominant structures in the ζ_1/f_0, Q_1, $w_{1.5}$ and K_{1t} fields at day 130 indicate that uncertainties can be attached to the task of extracting information from local dynamical balances also in the case when physical processes without strong signatures are present.

We point out that CTZ surface drifter tracks in late July 1988 give some indication that a meander in the CTZ jet has pinched off to form a detached cyclonic eddy with scales of order 150-200 km near 36.5°N, 126.5°W, offshore of the region of the CTZ hydrographic and ADCP surveys (see the discussion and Figure 7*c* of *Strub et al.* [this issue]).

5. Long Channel Experiment (LC)

To examine the finite amplitude behavior of the CTZ jet in a geometry where several along-jet wavelengths for linearly unstable modes are possible and where the initial disturbances are imposed in a somewhat more oceanographically relevant manner, we present results from one experiment in a long channel with $L^{(x)} = 1280$ km and $L^{(y)} = 650$ km. In this case, designated LC, the initial condition is $\psi_n(x, y, 0) = \psi_{0n}(y)$, and small disturbances are forced, as described in section 3, by

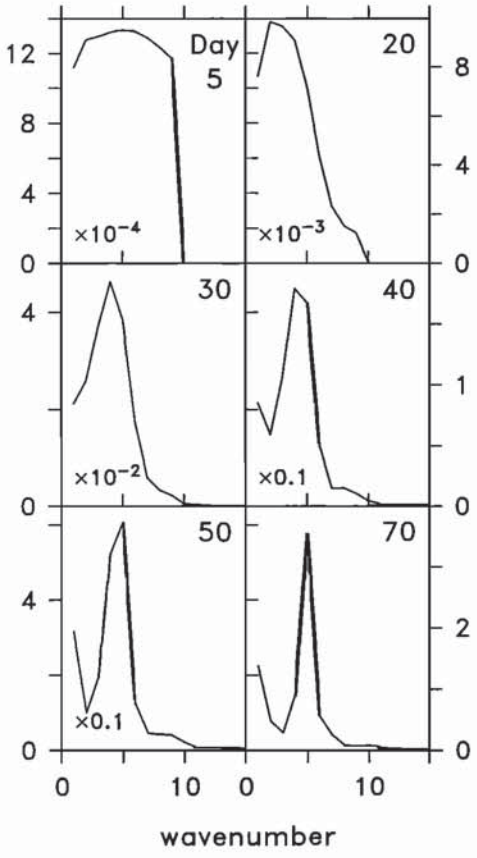

Fig. 14. The total energy $K + A = C[\{K\} + \{A\}]$, where $C = (L^{(x)}L^{(y)})^{-1}$, as a function of along-channel wavenumber for days 5, 20, 30, 40, 50, and 70 from experiment LC calculated from a Fourier decomposition in x of the velocity and interface displacement fields. Note the different scale factors for the energy for each day (given in the lower left corner of the panels).

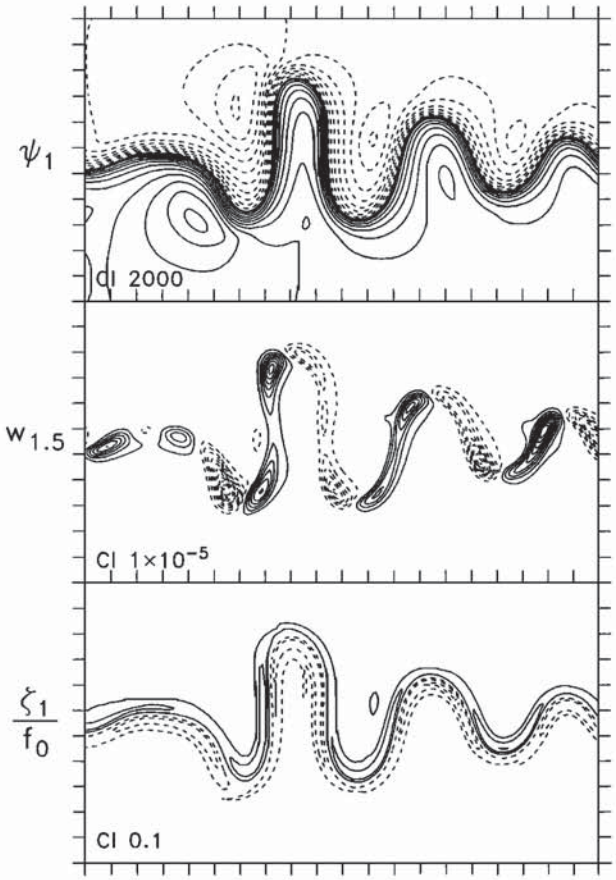

Fig. 15. Contour plots of the $\psi_1, w_{1.5}$, and ζ_1/f_0 fields as a function of (x, y) for day 70 from experiment LC with $L^{(x)} =$ 1280 km and $L^{(y)} = 650$ km. The fields are shown for $0 \leq x \leq$ 1000 km and 50 km $\leq y \leq$ 600 km. The distance between tick marks on the axes is 50 km.

a weak wind stress curl that acts over a period of 3 days. The curl of the wind stress (41) directly forces disturbances with along-channel wavenumbers 1–9 corresponding to along-channel wavelengths of 1280, 640, 426.7, 320, 256, 213.3, 182.9, 160, 142.2 km, respectively. The linear stability analysis in part 1 shows that disturbances with wavelengths corresponding to wavenumbers 2–9 are unstable. Wavenumber 5 corresponds to the wavelength (256 km) closest to that of the most unstable linear mode. The variation with m of the wind stress amplitude τ_{0m} is chosen artificially and empirically so that in an along-channel Fourier decomposition of the velocity and interface fields there is nearly equal total energy $\{K\}+\{A\}$ in each of the along-channel wavenumbers 1–9 at day 5 (Figure 14).

The fields of $\psi_1, w_{1.5}$, and ζ_1/f_0 at day 70 are shown in Figure 15, and those for $\psi_4, w_{4.5}$, and Q_4 are shown in Figure 16. Contour plots of the corresponding kinetic energy terms K_1, K_{1t}, dK_1/dt and $K_4, dK_4/dt, -b_4$ are given in Figures 17 and 18, respectively. Note that to save space, the fields are shown for $0 \leq x \leq 1000$ km and 50 km $\leq y \leq 600$ km, whereas in the calculation, $L^{(x)} = 1280$ km and $L^{(y)} = 650$ km. The figures omit only a small-amplitude sinusoidal meander between $x = 1000$ and $x = 1280$ km with characteristics very similar to the one between $x = 750$ and $x = 1000$ km. The day 70 fields were chosen because the finite amplitude meanders in the jet that are evident in Figures 15–18 are generally similar in amplitude to the CTZ jet meanders observed during the spring 1987 hydrographic and ADCP surveys [*Kosro et al.*, this issue] and represented in the CTZ data assimilation studies of *Walstad et al.* [this issue].

The amplitudes and the wavelengths of the day 70 meanders (Figures 15–18) vary in x along the channel in response to the specific spatial variability of the initial wind stress forcing in (41). The dependence of the total energy $\{K\} + \{A\}$ on the along-channel wavenumbers in a Fourier decomposition of the velocity and interface fields is shown for days 5, 20, 30, 40, 50 and 70 in Figure 14. At day 20, wavenumbers 1–5 contain the largest fraction of the energy, whereas at days 30, 40, and 50 most of the energy is in the two wavenumbers 4 and 5. At day 70 there is a high concentration of energy in the single wavenumber 5, which corresponds to the wavelength of the most unstable linear mode. Note that in connection with the relatively large amount of energy in wavenumber 4 for times through day 50, the linear stability results in part 1 show that perturbations with wavelengths of 320 km are unstable with growth rates not much less than the largest values found near wavelengths of 260 km. One clear result from Figure 14 is that there is relatively little growth of energy in the higher wavenumbers 7–9, although

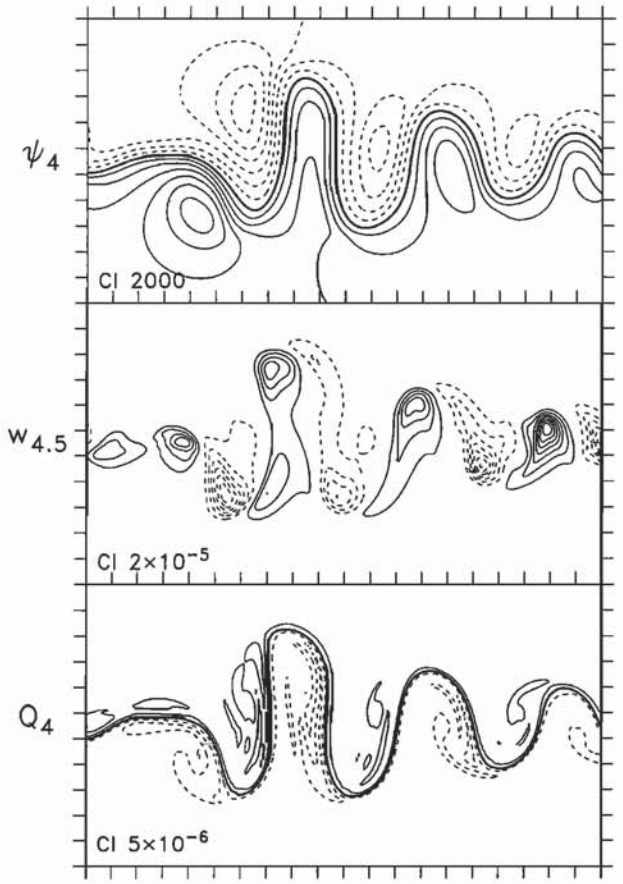

Fig. 16. Contour plots of the $\psi_4, w_{4.5}$, and Q_4 fields for day 70 from experiment LC. Scaling of axes as in Figure 15.

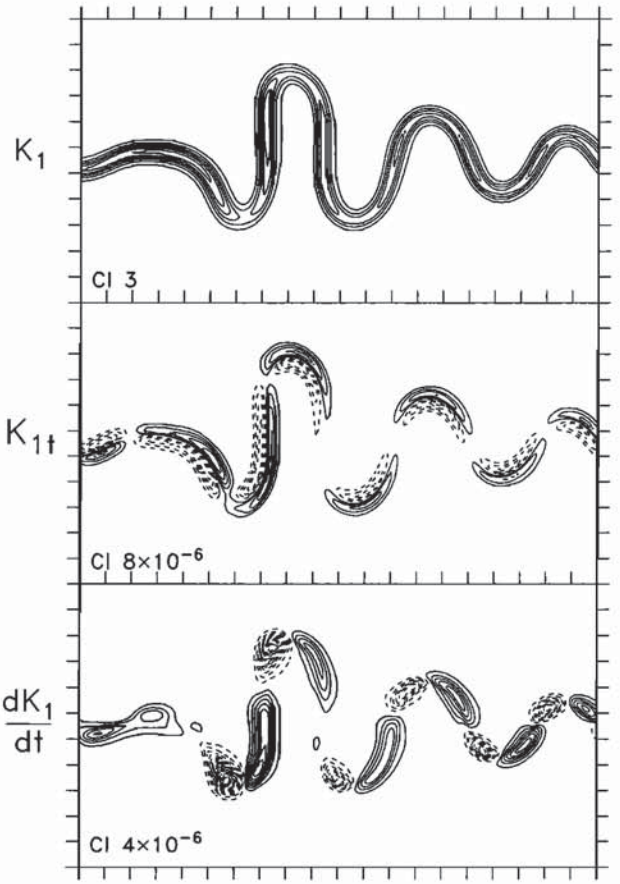

Fig. 17. Contour plots of the K_1, K_{1t}, and dK_1/dt fields for day 70 from experiment LC. Scaling of axes as in Figure 15.

these wavelengths of 182.9, 160, and 142.2 km are linearly unstable with growth rates at least two-thirds that of the maximum (part 1). The meander patterns in Figures 15–18 likewise visually indicate little relative energy growth at these smaller wavelengths. We examine further the finite amplitude behavior of disturbances at wavelengths 180 and 150 km in section 6.

The spatial structures of the $\psi_1, w_{1.5}$, and ζ_1/f_0 and the $\psi_4, w_{4.5}$, and Q_4 fields at day 70 from experiment LC in Figures 15 and 16 are very similar to those in the corresponding fields from the basic experiment BC for $t \leq 60$ days in Figures 2, 3, and 4, where in LC the variations in meander amplitude as a function of x along the channel correspond in BC to variations in the meander amplitudes as a function of time. For example, in LC the structure of the trough-to-trough portion of the meanders approximately centered on the crests near $x = 400$, 675, and 920 km corresponds roughly to the fields in BC at days 60, 50 and 40 days, respectively. An exception to this correspondence occurs in LC at $x \simeq 125$ km where in $w_{1.5}$ (Figure 15) there is a very small region of negative vertical velocities between two larger regions of positive values and in ψ_1 there is a corresponding decrease in curvature, or a flattening, of the jet axis. This feature is the result of an initial smaller scale along-jet disturbance of about 160 km at day 50 being compressed at day 70 between the large amplitude, more slowly moving meander with trough at $x \simeq 300$ km and a more rapidly propagating, larger along-jet scale meander with trough at $x \simeq 0$ km. Similar observations regarding the correspondence of LC and BC results may be made for the kinetic energy terms in Figures 17 and 18. In particular, the spatial variations of the dK_1/dt, dK_4/dt, and $-b_4$ terms in LC are close to those found in the basic experiment BC with similar differences between dK_1/dt and dK_4/dt and with similar structure in $-b_4$. Again, variations in x in LC correspond to variations in t in BC. The time variation in LC of the total, volume-integrated kinetic and potential energies and of the integrated energy conversion terms for $t \leq 70$ days is found to be qualitatively similar to that found in Figures 10, 11, and 12 for experiment BC for $t \leq 50$ days and is not shown.

Consequently, we find that the general behavior of the stream function, vertical velocity, and vorticity fields and of the kinetic energy terms found in the basic experiment BC in section 4 is also evident in the more general situation represented in experiment LC. As a result, the structural characteristics of those fields, previously discussed in section 4, may be useful as indicators of jet instability processes in regional open ocean models. Of course, in typical applications of regional models several physical processes may be active. For example, in the CTZ experiment [*Walstad et al.*, this issue] the jet generally winds its way through an evolving eddy field. In such situations, the presence of specific local balance signatures found in idealized cases may be obscured. Difficulties in this

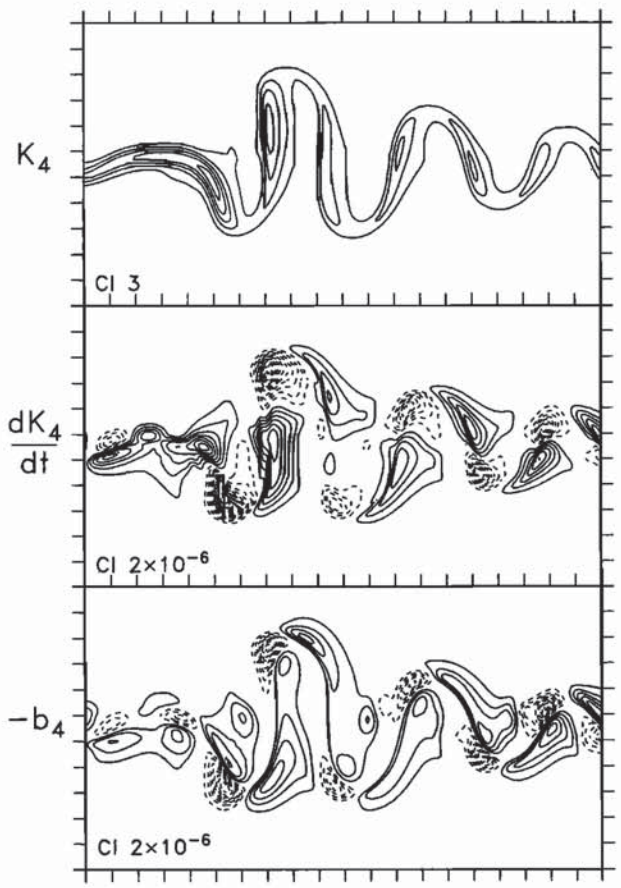

Fig. 18. Contour plots of the $K_4, dK_4/dt$, and $-b_4$ fields for day 70 from experiment LC. Scaling of axes as in Figure 15.

regard, when either the flow evolves in a complex manner accompanied by large local spatial and temporal variations in terms (as in days 90–110 in BC) or when strong signals of particular processes are absent (as in day 130 in BC), are discussed in section 4.2.

We note that although the meanders in LC at day 70 are generally similar to those found in the spring 1987 CTZ surveys, the observed jet [*Kosro et al.*, this issue; *Walstad et al.*, this issue] shows some evidence of relatively more energy in smaller scale meanders with wavelengths of order 150 km. The reasons for this are not clear but could be related to the greater complexity of the oceanographic situation involving, e.g., the interaction of the jet with an eddy field.

6. Other Experiments

To help in the interpretation of the results from the long channel experiment LC, where $L^{(x)} = 1280$ km and disturbances are excited initially with along-channel wavenumbers 1–9 but where relatively little growth of energy is observed in wavenumbers 7–9 (wavelengths 182.9, 160, 142.2 km), we conduct a set of experiments similar to the basic case BC, but with different values of $L^{(x)} = 180$ and 150 km. The experiments are listed in Table 2. In these cases, initial values for $\psi_n(x, y, 0)$ given by (40) are utilized where $\psi_{1n}(x, y)$, the perturbation to $\psi_{0n}(y)$, has the structure of the most unstable linear mode (as found in part 1) with wavelength equal to the chosen value of $L^{(x)}$. The amplitude of the initial perturbation $\psi_{1n}(x, y)$ is varied in different experiments.

The results of experiments with $L^{(x)} = 180$ and 150 km show different qualitative behavior than BC. The amplitudes of the jet meanders, rather than continuously increasing in magnitude until the meanders pinch off to form eddies, typically grow to some finite limit, usually less than about 50 km, and then exhibit regular or irregular time-dependent fluctuations that may asymptotically approach a state that is nearly steady or a state with time-dependent oscillations of $\{K\}$ and $\{A\}$. In order to get a more complete picture of the time variability and the large time asymptotic behavior of the instability in these numerical experiments, we calculate the solutions for much longer time periods than for the basic experiment BC, i.e., for 600 days.

We first consider experiment 180a (Table 2) with $L^{(x)} = 180$ km. The time variations of the integrated kinetic and potential energy terms are plotted in Figure 19. Also shown in Figure 19 are the time variations of the energy conversion terms $\{KP\}, \{AP\}$, and $-\{b\}$. The total energy $\{K\} + \{A\}$ decreases slowly with time due to the presence in (24) of weak dissipation associated with the biharmonic horizontal friction. The change in total energy $\{K\} + \{A\}$ over 600 days, however, is very small compared to the initial kinetic energy, reflecting the weak overall integrated effect of the friction forces. The total kinetic energy $\{\hat{K}\}$ in the perturbations increases initially for about 50 days and then starts to oscillate somewhat irregularly with a period of around 70 days about a level roughly equal to twice its

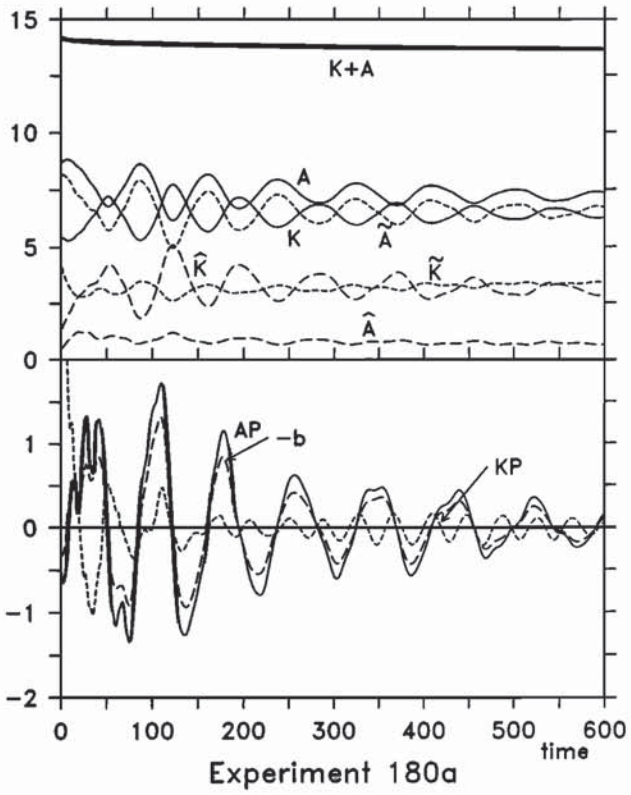

Fig. 19. Time variations in the volume integrated energy and energy conversion terms from experiment 180a with $L^{(x)} = 180$ km (Table 2). Variables defined as in Figure 10.

initial value. After day 120, the oscillations slowly decrease in magnitude and increase in period. The fluctuations in $\{\hat{K}\}$ are generally accompanied by similar variations in the total kinetic energy $\{K\}$ that are balanced by changes in total potential energy $\{A\}$. The variations in $\{A\}$ are primarily associated with variations in the potential energy $\{\tilde{A}\}$ of the x-averaged flow.

The layer 1 stream function ψ_1 and vorticity ζ_1/f_0 fields are plotted in Figure 20 for days 10, 80, 130, 340, and 350. The variations with time in the amplitude of the jet meanders are evident in the ψ_1 fields. The larger amplitudes, e.g., at day 130, correspond to the larger values of $\{\hat{K}\}$ in Figure 19 as expected. The along-jet propagation velocity of the meanders at days 340 and 350 may be seen from the ψ_1 fields and is $\simeq 4.5$ km d^{-1}. The vorticity field ζ_1/f_0 evolves such that the high (low) vorticity shed to the rear at the crest (trough) initially, as shown at day 10, appears at large times (day 340) centered between the crest and trough at the outer edge of the jet. The structure of the vorticity field at day 340 is reminiscent of some of the asymptotic large time states found by *Flierl et al.* [1987] for barotropic jets stabilized by the β effect.

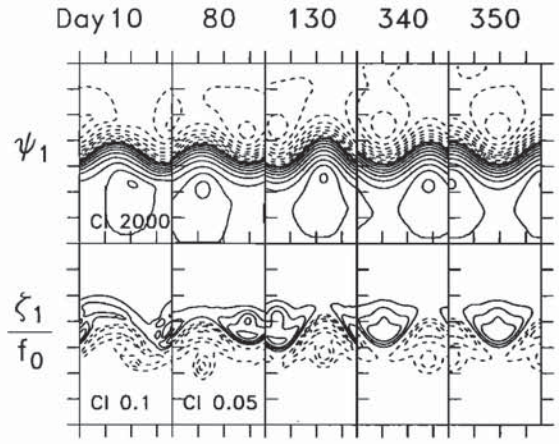

Fig. 20. Contour plots of the ψ_1 and ζ_1/f_0 fields at days 10, 80, 130, 340, and 350 from experiment 180a.

For the first 20 days the barotropic energy conversion term $\{KP\}$ (Figure 19) is positive and much greater in magnitude than the baroclinic conversion term $\{AP\}$ which is in fact negative for $t \leq 10$ days. We note that in part 1 the most unstable linear mode at wavelength 180 km comes from a different branch of the dispersion curve than the most unstable mode at wavelength 250 km. In the linear solution at 180 km wavelength, barotropic energy conversion processes associated with positive values of $\{KP\}$ dominate negative values of $\{AP\}$ consistent with the short time results here. After 15 days, $\{AP\}$ increases in magnitude so that it is comparable to, or larger than, $\{KP\}$. Oscillations in $\{AP\}$ and in $-\{b\}$ seem to play the major role in forcing the $\{\hat{K}\}$ fluctuations after day 100, although the amplitude of $\{KP\}$, which oscillates at about twice the frequency of $\{AP\}$, remains appreciable. For $t \geq 200$ days, oscillations in $\{AP\}$ and $-\{b\}$ appear to be associated primarily with exchanges in energy between the kinetic energy in the perturbations $\{\hat{K}\}$ and the potential energy in the x-averaged flow $\{\tilde{A}\}$. Similar to the results from the basic experiment BC for $t \leq 50$ days, the time variability of $\{AP\}$ in Figure 19 is closely followed by that of $-\{b\}$. That result is found in all of the experiments with $L^{(x)} = 180$ and 150 km.

In experiment 180b, the same parameters as in 180a are utilized, but the amplitude of the initial stream function perturbation $\psi_{1n}(x, y)$ in (40) is reduced in size (Table 2). The resulting time variations of the integrated kinetic and potential energy terms and of the integrated energy conversion terms are shown in Figure 21. The behavior is qualitatively similar to that in 180a except that in 180b the long time behavior for $t \geq 300$ days is dominated by smaller amplitude more regular oscillations in $\langle\hat{K}\rangle$ and $\langle\tilde{A}\rangle$ with a shorter period of about 60 days. The initial energy conversion for $t \leq 30$ days is provided by barotropic processes through $\{KP\}$, while $\{AP\}$ is negative. At large time $t \geq 350$ days, $\{KP\}$ decreases to relatively small values, and the oscillations in $\{\hat{K}\}$ and $\{\tilde{A}\}$ are forced by $\{AP\}$ and $-\{b\}$.

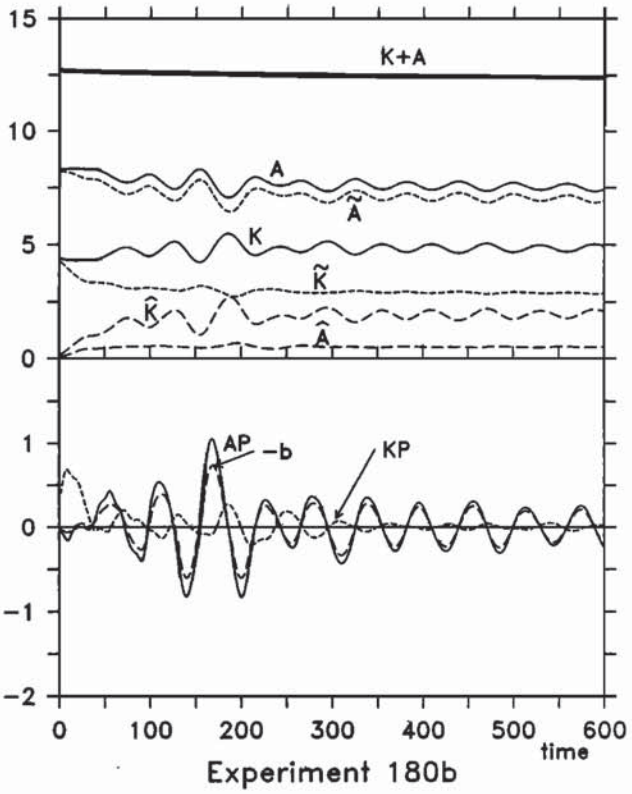

Fig. 21. As in Figure 19, but for experiment 180b.

In experiment 180c, in which the initial value of $\psi_{1n}(x, y)$ is intermediate in amplitude between that in 180a and 180b (Table 2), the flow curiously exhibits a large time behavior that is different than that found in 180a or 180b. For $t \leq 250$ days, the energy and energy conversion terms in 180c (Figure 22) vary as might be anticipated in a manner that is intermediate between that in 180a and 180b. For $t \geq 400$ days, however, the flow in 180c approaches a state with small and decreasing magnitudes of $\{KP\}, \{AP\}$, and $-\{b\}$ and with nearly steady, nonzero values of $\{\hat{K}\}, \{\hat{A}\}, \{\tilde{K}\}$, and $\{\tilde{A}\}$. Note that the large time limiting values of $\{A\}$ and $\{K\}$ are decreased and increased, respectively, with respect to their initial conditions.

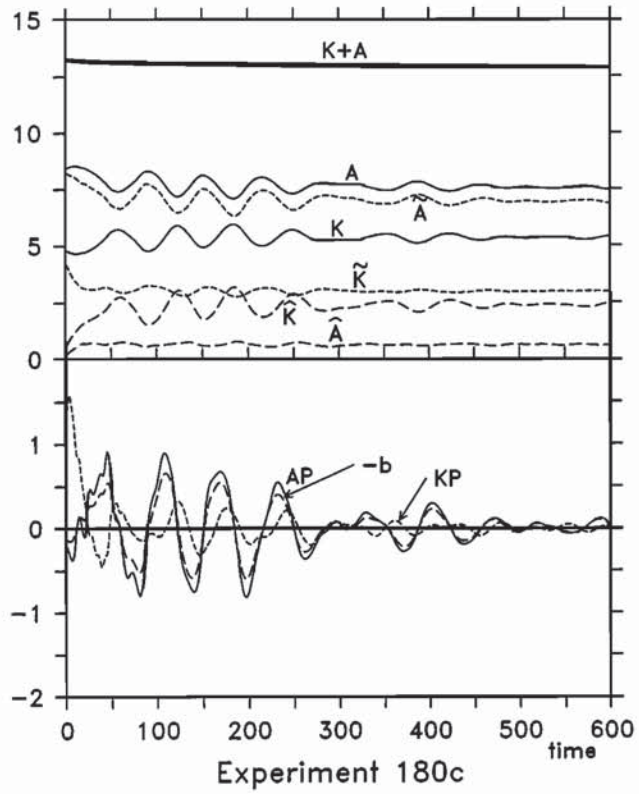

Fig. 22. As in Figure 19, but for experiment 180c.

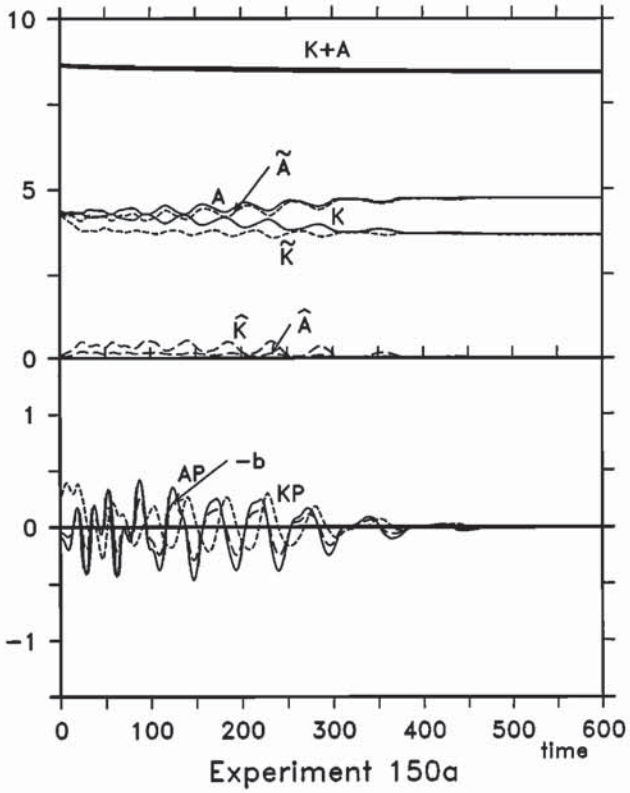

Fig. 23. Time variations in the volume integrated energy and energy conversion terms from experiment 150a with $L^{(x)} = 150$ km (Table 2). Variables defined as in Figure 10.

We also ran experiments with $L^{(x)} = 180$ km where the initial value of ψ_n is $\psi_{0n}(y)$ and the initial disturbances are forced by a short time application of wind stress curl as in (41) and (42) with $M = 1$. The resulting finite amplitude variability is qualitatively similar to that described above; that is, the amplitude of the meanders remains bounded and the flow exhibits time-dependent oscillatory or nearly steady behavior.

The first experiment 150a with $L^{(x)} = 150$ km shows initial growth of $\{\hat{K}\}$ (Figure 23) associated with positive values of $\{KP\}$ dominating negative values of $\{AP\}$. This is also consistent with the linear stability results in part 1 where the most unstable linear mode at 150 km is found to have properties similar to the mode at 180 km. The initial growth of $\{\hat{K}\}$ is followed by irregular oscillations in $\{\hat{K}\}$ with time scales of about 40 days in which $\{KP\}$ and $\{AP\}$ are out of phase but make comparable contributions to the energy conversion. Around day 375, the kinetic $\{\hat{K}\}$ and potential $\{\hat{A}\}$ energy in the perturbations decreases to near zero values, and the flow field asymptotically approaches a nearly steady x-independent jet structure. The profiles of the x-averaged velocity $\overline{u}_n(y,t)$ at large time $t = 600$ days are shown in Figure 24. In comparison with the initial values (Figure 1), they show a decrease in the maximum values in each layer, a general increase in the width of the mean jet, and the development in the upper layers of regions of negative velocities on the outer edges of the jet. Note that the asymptotic, large time state (Figure 23) is characterized by an increase in $\{A\}$ and a decrease in $\{K\}$ compared with the initial values. The large time $\overline{u}_n(y, t = 600)$ jet in Figure 24 appears to be stable to small disturbances. This is demonstrated by additional experiments in which these $\overline{u}_n(y, t = 600)$ profiles are used as initial conditions and disturbances are forced by a short time application of wind stress curl as in (41) and (42). The perturbed flow remains very close to the initial values, unlike with the original profiles in Figure 1 where the perturbations grow in a manner similar to that shown in Figure 23. In addition, application of the frictionless linear stability analysis of part 1 to $\overline{u}_n(y, t = 600)$ indicates a weak inviscid instability at 150 km wavelength with a large e-folding growth period of 340.9 days, which compares with a much shorter growth period of 17.7 days for the initial profiles in Figure 1.

In experiment 150b the initial amplitude of $\psi_{1n}(x, y)$ is increased (Table 2). In this case (not shown), the asymptotic large time behavior of the flow field for $t \geq 250$ days, rather than approaching a steady x-independent jet, involves a nearly periodic oscillation, primarily in $\{\hat{K}\}$ and $\{\tilde{A}\}$, of about 60 days period with most of the forcing provided by $\{AP\}$ and $-\{b\}$. The behavior is very similar to that shown for 180b in Figure 21 except that the large time oscillations in $\{A\}$ and $\{K\}$ in 150b are around levels that, as in 150a, are increased and decreased, respectively, compared with the initial values. This characteristic of the asymptotic behavior in the experiments with $L^{(x)} = 150$ km differs from the results of all of the cases with $L^{(x)} = 180$ km and of BC where generally $\{A\}$ decreases and $\{K\}$ increases.

The major qualitative difference in the results of the basic experiment BC with $L^{(x)} = 250$ km, where the amplitudes of the meanders continue to grow until eddies are pinched off, and of the experiments with $L^{(x)} = 180$ and 150 km, where the amplitudes of the meanders remain bounded offers some explanation for the structure of the finite amplitude meanders found at day 70 in experiment

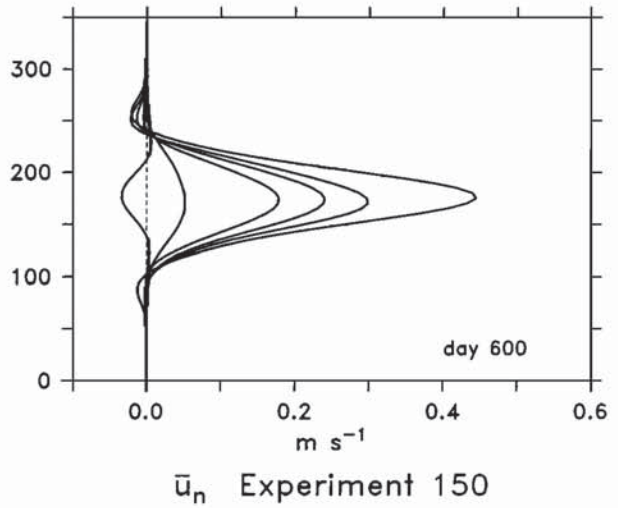

Fig. 24. The x-averaged velocities $\overline{u}_n$ as a function of y in km for day 600 in experiment 150a. The maximum velocity magnitudes decrease monotonically with depth.

LC which have relatively little energy at wavelengths of 182.9, 160, and 142.2 km. The difference in behavior also raises the question of what value of the along-jet wavelength generally divides these two types of response. This was investigated to some extent in further numerical experiments with $L^{(x)} = 200$ km where we found growth of meanders followed by single eddy detachment at the trough similar to that in BC. We note that 200 km is close to the smallest wavelength for which the initial unstable mode $\psi_{1n}(x, y)$ is of similar type to that for experiment BC, i.e., where it is from the same branch of the dispersion curve (part 1). The nature of the response with $L^{(x)} = 200$ km, however, was found to be extremely sensitive to the basic stratification. Other experiments with $L^{(x)} = 200$ km and identical parameter values, except that $g'_{5.5} = 0.363 \times 10^{-2}$ m s^{-2} (rather than $g'_{5.5} = 0.395 \times 10^{-2}$ m s^{-2} (Table 1)), and with the same properties in the initial conditions, produced solutions with bounded amplitude, time-dependent meanders.

The characteristics of the finite amplitude behavior of the CTZ jet found in the experiments with $L^{(y)} = 180$ and 150 km, that is, the asymptotic approach to nearly steady states or to irregular or nearly periodic oscillations in $\{\hat{K}\}$, are similar to the flow characteristics predicted by idealized theoretical models for weakly nonlinear baroclinic instability in a two-layer fluid [e.g., *Pedlosky*, 1987, section 7.16]. The present results are interesting from a geophysical fluid dynamics point of view, coming as they do from solutions of the fully nonlinear quasi-geostrophic partial differential equations with initial conditions extracted from oceanographic observations. Nevertheless, the importance of this behavior to a physical interpretation of the CTZ measurements is not clear given that for the particular CTZ jet studied here instabilities with along-jet wavelengths between at least 200 and 320 km are found to lead to large-amplitude growing meanders that dominate the flow behavior in geometries where they are allowed, e.g., in experiment LC. For that reason, although the dynamics and parameter dependence of the instability processes found in the experiments in this section are of independent interest and warrant further study, we do not pursue that here.

7. SUMMARY

The results of experiments BC with $L^{(x)} = 250$ km for $t \leq 60$ days and LC with $L^{(x)} = 1280$ km for $t \leq 70$ days show the growth and development of finite amplitude meanders in the CTZ jet similar to those observed in the CTZ field experiment in spring 1987. The ψ_n, ζ_n/f_0, $w_{n+\frac{1}{2}}$, Q_n, and K_n fields for $n = 1$ and $n = 4$ at day 70 in LC have similar spatial structure to the fields of the same variables in BC for $t \leq 60$ days, where variations in x in LC correspond to variations in t in BC. The same observation holds for the kinetic energy balance terms K_{1t}, dK_1/dt, dK_4/dt, and $-b_4$. The vertical velocity fields $w_{1.5}$ and $w_{4.5}$ develop a characteristic spatial structure that involves positive $w_{n+\frac{1}{2}}$ for fluid particles moving from troughs to crests and negative $w_{n+\frac{1}{2}}$ for particles moving from crests to troughs (Figures 2, 4, 15, and 16) consistent with the increase with time of positive vorticity in the troughs and negative vorticity in the crests (Figures 2 and 15). The largest-magnitude vertical velocities are found centered between crests and troughs in the small-amplitude meanders but appear just ahead of the crests and troughs in the larger-amplitude meanders. The deeper vertical velocity field $w_{4.5}$ is larger in magnitude than $w_{1.5}$ and is spread over a larger region about the jet axis. The time rate of change of kinetic energy following fluid particles in layer 1, dK_1/dt (Figures 5 and 17), develops an organized spatial structure along the jet axis showing decreases (increases) in K_1 for fluid particles entering (leaving) the crests and troughs. In layer 4 (Figures 6 and 18), however, nonzero values of dK_4/dt are spread over a wider region about the jet axis and reflect the spatial structure of the conversion term $-b_4$ which is relatively large in layer 4. In LC at day 70, the conversion term $-b_4$ is positive over a great deal of the jet flow field (Figure 18), consistent with positive integrated values of $-\langle b_4 \rangle$. Local, large-magnitude negative values of $-b_4$ exist in small regions just ahead of the crests and troughs.

In BC, the instability starts with comparable integrated contributions from barotropic conversion processes $\{KP\}$ and from baroclinic conversion processes $\{AP\}$, consistent with the results of linear theory in part 1. After about day 30, however, when the amplitude of the meanders exceed 30 km, the magnitude of the baroclinic contributions of $\{AP\}$ greatly exceed the barotropic contributions of $\{KP\}$. The time variability of the integrated conversion term $-\{b\}$ is similar to that of $\{AP\}$ in BC for $t \leq 50$ days. Since $\langle b_n \rangle \neq 0$, this raises the possibility that the spatial and time variations of the energy conversion term $-b_n$ may provide an indicator for the presence of baroclinic instability processes in applications of open ocean, data assimilation models to the CTZ region. From an examination of the $-b_4$ fields in BC and LC (Figures 6, 9, and 18), we see that an identification of net positive contributions from the conversion term $-b_n$ in limited area model solutions may be difficult in general. Knowledge of the characteristic spatial distributions of the $-b_4$ fields found here may prove helpful, however.

At about $t = 70$ days in BC the growing meanders start to deform and to pinch off. The pinching-off process proceeds vigorously between days 90 and 110. By day 110 an elliptical, cyclonic eddy, with spatial scales of the major and minor axes equal to about 325 and 150 km, respectively, has essentially detached from the trough below the jet,

and a smaller more nearly circular anticyclonic eddy of diameter about 150 km has nearly detached from the crest. The pinching-off and detachment process during days 90 to 110 is characterized by the development of relatively large negative values of $\{KP\}$ and a corresponding sharp increase in $\{\tilde{K}\}$. After the eddies have detached, e.g., at day 130, the jet is wider $L_{J1} \simeq 100$ km, compared to an initial value of $L_{J1} \simeq 60$ km, and the flow field has developed substantially increased values of kinetic energy $\langle \tilde{K}_n \rangle$ in the bottom layers $n = 6$, 5, and 4 and corresponding decreased values of potential energies $\langle A_{n+\frac{1}{2}} \rangle$ for the lower $n = 4$ and 5 interfaces.

Results of numerical experiments with different values of $L^{(x)}$ show that qualitatively different behavior from that found in BC is obtained for smaller $L^{(x)} = 180$ and 150 km. In these cases, meanders grow, but the maximum value of their amplitude is limited to about 50 km. Depending on the experiment, the flow field may asymptotically approach for large time a nearly steady x-independent jet with the kinetic energy of the perturbations $\{\hat{K}\} \simeq 0$, a jet where $\{\hat{K}\}$ is nonzero and approximately constant in time, or to a flow where $\{\hat{K}\}$ and $\{\tilde{A}\}$ oscillate in a somewhat irregular or nearly periodic manner with time scales from 50 to 100 days. In experiments, such as LC, where the geometry allows the existence of longer along-jet wavelengths associated with growing meanders, the resulting growth at those wavelengths dominates the development of the flow field. The bounded amplitude time-dependent behavior found for $L^{(x)} \leq 180$ km is not seen but helps to explain the relatively small energy at wavelengths 182.9, 160, and 142.2 km found in the meanders for days 20 to 70 in LC.

Acknowledgments. This research was supported by the Office of Naval Research Coastal Sciences Program under contracts N00014-87-K-0009 and N00014-90-J-1051 and by the National Science Foundation under grants OCE-8620403 and OCE-9013263. Computer resources at the National Center for Atmospheric Research (NCAR) were utilized under Project 35271038. NCAR is funded by the National Science Foundation. The authors are particularly grateful to W. R. Holland and J. H. S. Chow for providing the quasi-geostrophic, multilayer, numerical, finite difference channel model. They also thank S. D. Pierce for computations of the linear instability modes and F. Beyer for typing the manuscript.

REFERENCES

Bower, A. S., and T. Rossby, Evidence of cross-frontal exchange processes in the Gulf Stream based on isopycnal RAFOS float data, *J. Phys. Oceanogr.*, *19*, 1177–1190, 1989.

Flierl, G. R., and A. R. Robinson, On the time-dependent meandering of a thin jet, *J. Phys. Oceanogr.*, *14*, 412–423, 1984.

Flierl, G. R., P. Malanotte-Rizolli, and N. J. Zabusky, Nonlinear waves and coherent vortex structures in barotropic β-plane jets, *J. Phys. Oceanogr.*, *17*, 1408–1438, 1987.

Holland, W. R., The role of mesoscale eddies in the general circulation of the ocean-numerical experiments using a wind-driven quasigeostrophic model, *J. Phys. Oceanogr.*, **8**, 363–392, 1978.

Huyer, A., et al., Currents and water masses of the coastal transition zone off northern California, June to August 1988, *J. Geophys. Res.*, this issue.

Ikeda, M., Meanders and detached eddies of a strong eastward-flowing jet using a two-layer quasi-geostrophic model, *J. Phys. Oceanogr.*, *11*, 526–540, 1981.

Ikeda, J., and J. R. Apel, Mesoscale eddies detached from spatially growing meanders in an eastward-flowing oceanic jet using a two-layer quasi-geostrophic model, *J. Phys. Oceanogr.*, *11*, 1638–1661, 1981.

Kadko, D. C., L. Washburn, and B. Jones, Evidence of subduction within cold filaments of the Northern California coastal transition zone, *J. Geophys. Res.*, this issue.

Kosro, P. M., et al., The structure of the transition zone between coastal waters and the open ocean off northern California, winter and spring 1987, *J. Geophys. Res.*, this issue.

McWilliams, J. C., A note on a consistent quasi-geostrophic model in a multiply connected domain, *Dyn. Atmos. Oceans*, **1**, 427–441, 1977.

McWilliams, J. C., W. R. Holland, and J. H. Chow, A description of numerical Antarctic Circumpolar Currents, *Dyn. Atmos. Oceans*, **2**, 213–291, 1978.

Meacham, S. P., Meander evolution on quasi-geostrophic jets, *J. Phys. Oceanogr.*, in press , **1991.**

Pedlosky, J., *Geophysical Fluid Dynamics*, 710 pp., Springer-Verlag, New York, 1987.

Pierce, S. D., J. S. Allen, and L. J. Walstad, Dynamics of the coastal transition zone jet, 1. Linear stability analysis, *J. Geophys. Res.*, this issue.

Pinardi, N., and A. R. Robinson, Quasi-geostrophic energetics of open ocean regions, *Dyn. Atmos. Oceans*, *10*, 185–219, 1986.

Pratt, L. J., Meandering and eddy detachment according to a simple (looking) path equation, *J. Phys. Oceanogr.*, *18*, 1627–1640, 1988.

Pratt, L. J., and M. E. Stern, Dynamics of potential vorticity fronts and eddy detachment, *J. Phys. Oceanogr.*, *16*, 1101–1120, 1986.

Robinson, A. R., M. A. Spall, and N. Pinardi, Gulf Stream simulations and the dynamics of ring and meander processes, *J. Phys. Oceanogr.*, *18*, 1811–1853, 1988.

Spall, M. A., and A. R. Robinson, Regional primitive equation studies of the Gulf Stream meander and ring formation region, *J. Phys. Oceanogr.*, *20*, 985–1016, 1990.

Strub, P. T., et al., The nature of the cold filaments in the California Current system, *J. Geophys. Res.*, this issue.

Walstad, L. J., J. S. Allen, P. M. Kosro, and A. Huyer, Dynamics of the coastal transition zone in 1987 through data assimilation studies, *J. Geophys. Res.*, this issue.

Washburn, L., D. C. Kadko, B. H. Jones, T. Haywood, P. M. Kosro, T. P. Stanton, S. Ramp, and T. Cowles, Water mass subduction and the transport of phytoplankton in a coastal upwelling system, *J. Geophys. Res.*, this issue.

J. S. Allen, P. A. Newberger, and L. J. Walstad, College of Oceanography, Oregon State University, Oceanography Admin Bldg 104, Corvallis, OR 97331-5503.

(Received January 14, 1991;
accepted March 21, 1991.)